Investigating X-ray variability of AGN through spectral and temporal analyses: Mrk 530 & Mrk 335

by

Hannah Jae Sariah Ehler

A Thesis Submitted to Saint Mary's University, Halifax, Nova Scotia in Partial Fulfillment
of the Requirements for the Degree of MSc in Astronomy
(Department of Astronomy and Physics)

2019, Halifax, Nova Scotia

Approved: _____

Dr. Luigi Gallo (Advisor)

Approved: _____

Dr. Philip Bennett (Examiner)

Approved: _____

Dr. Roby Austin (Examiner)

Date: August 16, 2019.

Acknowledgements

I wish to thank my supervisor Dr. Luigi Gallo for his guidance and patience over the past four years, and for helping me become the scientist I am today. I would also like to thank Adam Gonzalez for his support, and Finnegan and Xena for making me take breaks and helping me stay positive.

I would also like to thank the anonymous MNRAS referee of our Mrk 530 paper for their careful reading and helpful comments on the original manuscript, as well Dr. Roby Austin and Dr. Phil Bennett for taking the time to be part of this process.

Contents

List of Figures

List of Tables

Abstract

Investigating X-ray variability of AGN through spectral and temporal analyses: Mrk 530 & Mrk 335

by Hannah Ehler

X-ray observations of two Seyfert AGN were analysed in an effort to characterise the nature of their variability. A spectral analysis was performed on a *Suzaku* observation of the Seyfert 1.5 AGN Mrk 530, and a timing analysis on *XMM-Newton* observations of the narrow-line Seyfert 1 Mrk 335. Mrk 530 was found to exhibit two distinct spectral states over the course of a single observation, as well as apparent periodic variability in the light curve. Three physical models (blurred reflection, partial covering, and soft Comptonisation) were explored to characterise the spectrum however the spectral fits were indistinguishable. The timing analysis of Mrk 335 revealed evidence of non-stationary behaviour using multiple timing methods, though it is difficult to determine if these results are real or artifacts of undersampling. As such, further testing is required to confirm these results.

August 16, 2019

Chapter 1

Introduction

1.1 Active Galactic Nuclei

It is thought that most, if not all, galaxies harbour a supermassive black hole at their centre, which can range in mass from $\sim 10^6 - 10^9$ $M_\odot$. In a small fraction ($\lesssim 1\%$) of these black holes, their surroundings are emitting radiation and so are called Active Galactic Nuclei, or AGN. These objects are among the most energetic in the Universe. They are so incredibly bright that they can outshine the stellar light of the host galaxy in which they reside, and emit radiation across the electromagnetic spectrum, from radio to gamma-ray waves. The spectral energy distribution (SED) of an AGN (Figure 1.1) varies between different types of AGN, but key components remain consistent. Various processes contribute to the SED and approximately equal amounts of energy are emitted in each waveband. The peak emission of an AGN is in the ultraviolet part of the spectrum, however we are unable to observe this peak due to absorption from gas and dust in our own Galaxy.

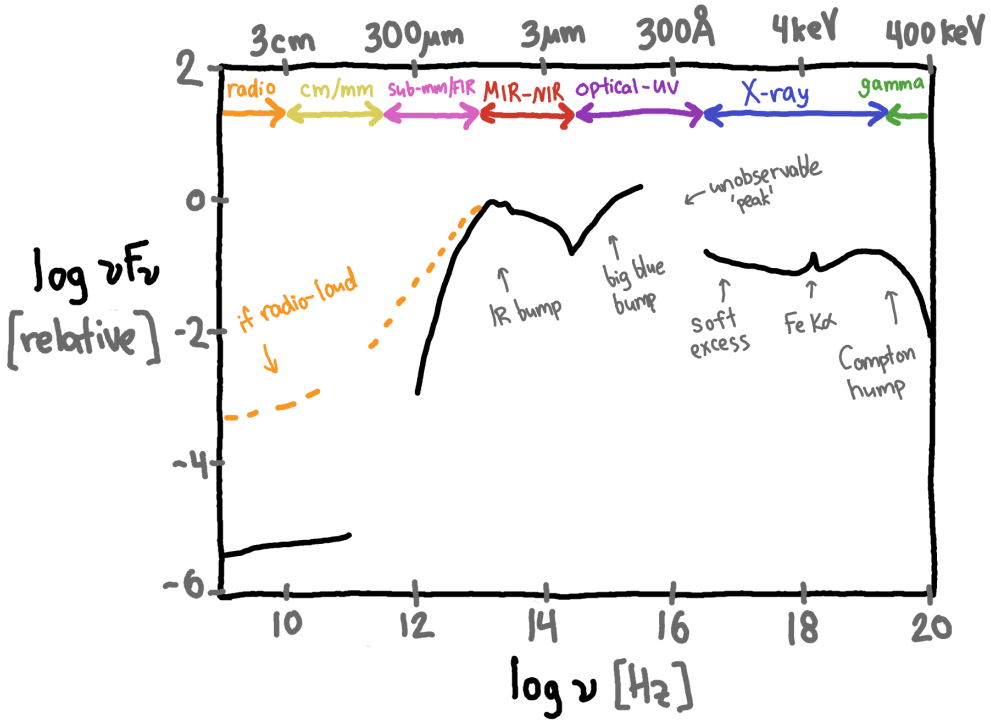

Figure 1.1: Spectral energy distribution (SED) of an unobscured (Seyfert 1) AGN. (Reproduced from Harrison 2014.)

AGN are some of the most energetic objects in the known Universe, with bolometric luminosities up to $\sim 10^{13}$ $L_{\odot}$ and higher. Their emission is thought to be powered by an accretion disc made up of hot gas and dust that surrounds the black hole. As material in the disc spirals in towards the black hole, it loses angular momentum and gravitational potential energy. As per the virial theorem, half of the gravitational potential energy is converted into kinetic energy while the other half is converted to radiation, powering the AGN emission. The efficiency of converting matter to energy through accretion onto black holes is between $5.7 - 40\%$ (Gallo 2011). For comparison, the radiative efficiency from nuclear fusion of H into He (the proton-proton chain) is 0.66%. There is also a complex interaction between the material in the disc and the magnetic field structure surrounding the black hole which contributes to this powerful emission, however, this interaction is currently not well understood.

Studying the radiation emitted from active galactic nuclei allows us to learn about things such as the accretion process, matter in extreme gravitational and magnetic fields, black hole growth, and the importance of black holes in galaxy evolution.

1.2 Unified Model

Active Galactic Nuclei were first classified by Seyfert (1943) based on their optical emission lines. Since then, there have been additional classifications based on characteristics such as radio emission, gamma-ray emission, spectral shapes, and emission line widths. The Unified Model posits that fundamentally these objects are all the same, powered by the same central engine and accretion process; the only difference between these types is the angle at which they are observed relative to Earth.

The generally accepted model of an AGN (Figure 1.2) consists of a supermassive black hole with a mass ranging from $\sim 10^6$ to 10^9 $M_\odot$. This black hole is surrounded by an accretion disc for which the model by Shakura & Sunyaev (1973) is commonly adopted. Their model describes a geometrically thin disc composed of hot gas that is optically thick such that the material composing the disc radiates like a blackbody. In this simple model, the AGN luminosity is derived entirely from accretion and is emitted locally before it can accrete inward. More complex models of the accretion disc have since been presented (e.g. Novikov & Thorne 1973; Madau 1988; Narayan & McClintock 2008), but the standard accretion disc model of Shakura & Sunyaev (1973) is a reasonable approximation. The accretion disc can extend out to ~ 1000 r_g (gravitational radii; $r_g = GM/c^2$) from the black hole (Netzer 2013), with the temperature decreasing with radius. The black hole and accretion disc form what is referred to as the 'central engine'.

Interior to the torus lies the broad-line region. This region is affected by the gravitational potential well of the black hole, and so any emission or absorption lines originating from

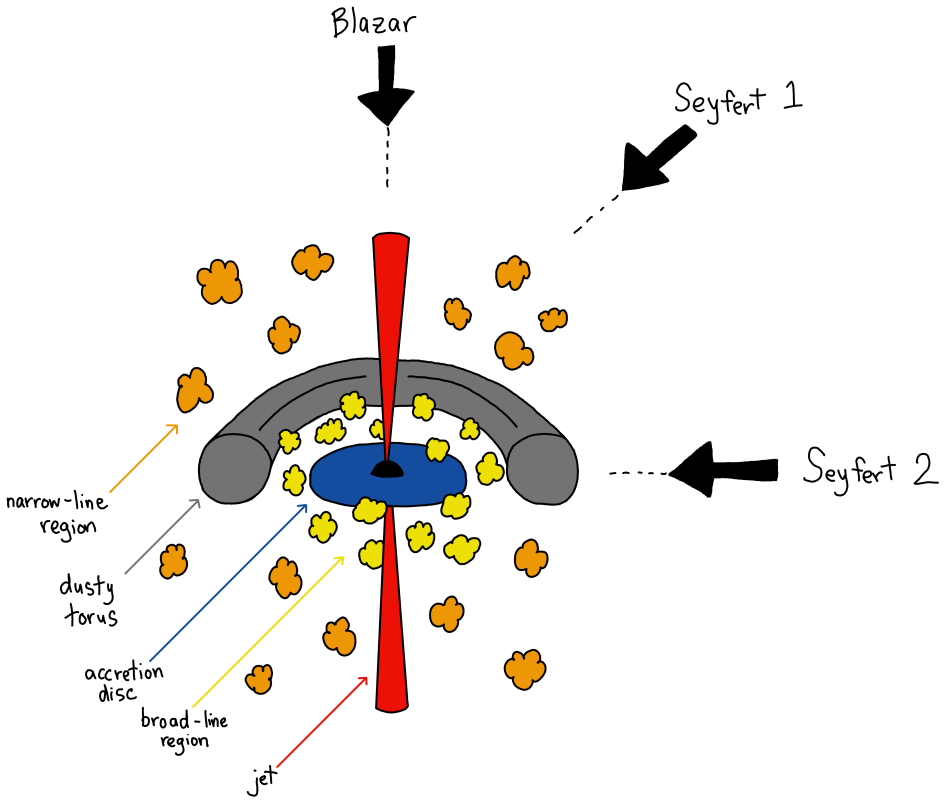

Figure 1.2: Schematic of an AGN noting the classification of the AGN based on the viewing angle as per the unified model. The entire system scales with luminosity and black hole mass. (Not to scale.)

this region will be Doppler broadened from motion around the black hole. The broad-line region extends $\sim 0.1 - 1$ pc from the black hole and scales with luminosity. The typical Keplerian velocity in this region is ~ 3000 km s^{-1} (Netzer 2013).

At further radii ($\sim 0.1 - 10$ pc) resides the torus, an optically thick ring of gas and dust that obscures the central region from certain angles. The torus emits radiation in the infrared regime and obscures and scatters X-ray emission from the central region because of its high column densities. Keplerian velocities in this region are ~ 1000 km s^{-1} (Netzer 2013).

Beyond the torus and on galactic scales lies the narrow-line region. This region is illuminated by the central engine but is free from the influence of the black hole's gravitational potential; thus, emission lines produced from this region are narrow. Like the broad-line region, there are likely clouds of gas and dust in this region. The narrow-line region can extend up to ~ 3000 pc from the black hole (Netzer 2013).

Some AGN feature a jet which extends along the black hole spin axis, perpendicular to the accretion disc. These jets are composed of relativistic gas flowing outward from the black hole and confined by magnetic fields. These are dominant in radio emission and can fill the space between galaxies.

The inclination that an AGN is observed at determines the type of AGN that is seen and how it is classified (Figure 1.2). For example, if an AGN harbouring a jet is viewed jet-on, the emission is heavily beamed toward the observer and it appears incredibly bright; this is classified as a blazar. The classifications most relevant to this work are Seyfert galaxies (Seyfert 1943). These are spiral galaxies with strong emission lines in their optical spectra.

Seyfert galaxies are further classified as Seyfert 1 and Seyfert 2 types.

Seyfert 1 (a.k.a. Type 1) AGN are systems for which we have an unobscured view of the central region, as the dusty torus is not along our line-of-sight. Seyfert 1 optical/UV spectra exhibit both narrow and broad emission lines as the broadening effect of the central region is visible. Seyfert 2 (a.k.a Type 2) AGN are systems whose central region is completely obscured by the torus as we are viewing the torus edge-on. These spectra contain only narrow emission lines as the broadening effect of the central region is obscured. There can also exist intermediate-type Seyferts (e.g. Seyfert 1.2, 1.5, 1.8) which bear characteristics akin to both Type 1 and Type 2 sources, with varying levels of obscuration.

Observations of Type 1 AGN reveal the central most regions of the black hole system where the X-rays are generated. These types of objects are of interest in this work.

1.3 X-ray Emitting Region

1.3.1 X-ray Observations of AGN

The central engines of AGN are not resolved with current X-ray telescopes and so appear only as point sources in our observations; we cannot resolve the central region. This means that we can detect no spatial information about the photons collected. For each photon received by the detector, the instrument is able to record the time of detection and the energy of the photon. The timing information is used to construct light curves (plots of the flux or photon counts over time), and the energy information is used to create spectra (plots of the flux or photon counts over energy). Analyses carried out on these light curves and spectra allow us to indirectly infer the geometry, scales, and processes of the inner region of the AGN, though these cannot be directly observed.

AGN emit light across the entire electromagnetic spectrum. Approximately 10% of the total energy budget of an AGN is emitted in the X-rays (Kolb 2010). We know from light travel-time effects that the X-rays are emitted in a very compact region close to the black hole. We observe rapid variations in X-ray emission on the scale of minutes to hours, and can thus infer the size of the emitting region as changes in emission cannot occur faster than the time it takes light to travel across the region. The X-ray emitting region of a 10^7 $M_\odot$ black hole is approximately the size of our solar system (Gallo 2011).

1.3.2 Geometry of the Central X-ray Emitting Region

Our current understanding of the geometry of the inner region of AGN (Figure 1.3) consists of a supermassive black hole surrounded by an accretion disc. The accretion disc is composed of hot gas orbiting the black hole, which emits radiation (through differential rotation and viscosity) in the form of ultraviolet photons. At some height above the black hole lies the corona, a hot cloud of free electrons with temperatures $\gtrsim 10^9$ K. The geometry of the corona is yet to be constrained, with some studies suggesting point-like sources (e.g. Wilkins & Fabian 2012), collimated (e.g. Wilkins & Gallo 2015a; Gonzalez et al. 2017), extended (e.g. Gonzalez et al. 2017), or patchy structures (e.g. Wilkins & Gallo 2015b), or even the base of a jet (e.g. Gonzalez et al. 2017). Ultraviolet photons emitted from the accretion disc interact with the corona and are up-scattered to higher energies through the process of Comptonisation (inverse Compton-scattering). The photons gain energy and are emitted from the corona as X-rays, constituting the primary X-ray emission in AGN. This emission takes the shape of a power-law on account of the Compotonisation process that produced it (Figure 1.4). This power-law has a cutoff at some energy, which indicates the temperature of the corona.

The primary emission from the corona is emitted isotropically, so some of the X-rays are emitted back towards the accretion disc. These photons are scattered off of the accretion disc, which is cooler and thicker than the corona. These scattered photons comprise the reflected emission, which bears signatures from the accretion disc such as emission lines, Doppler broadening, and relativistic blurring. Emission lines from the gas in the accretion

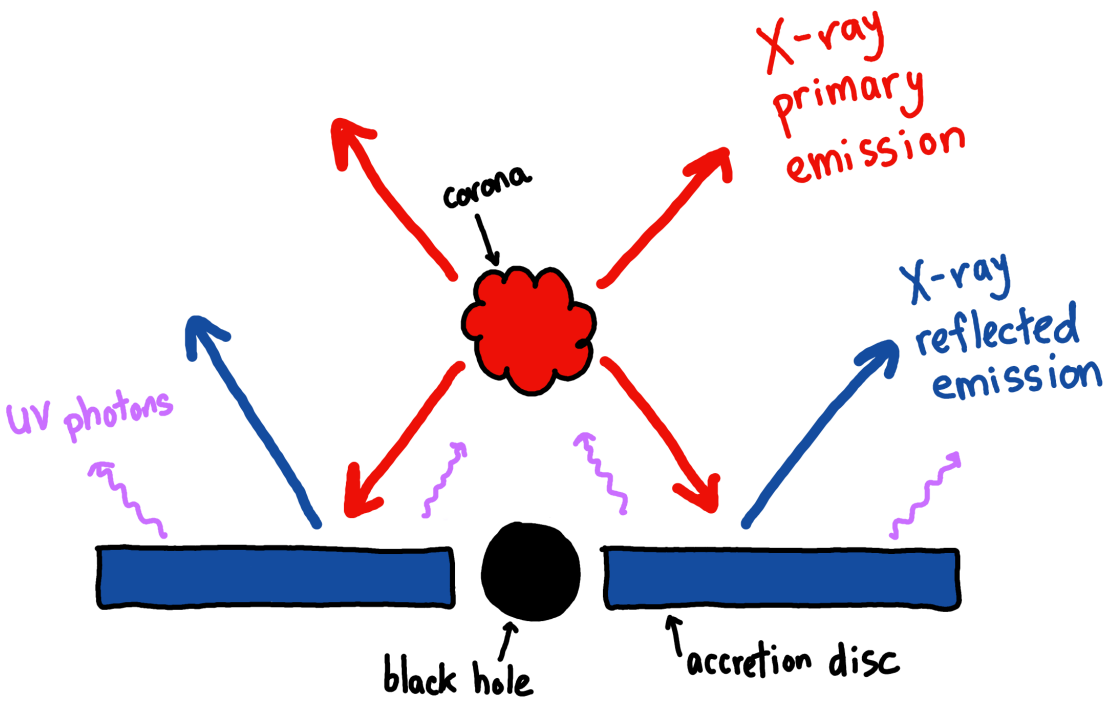

Figure 1.3: Schematic of the central region of an AGN. (Reproduced from Gallo 2011.)

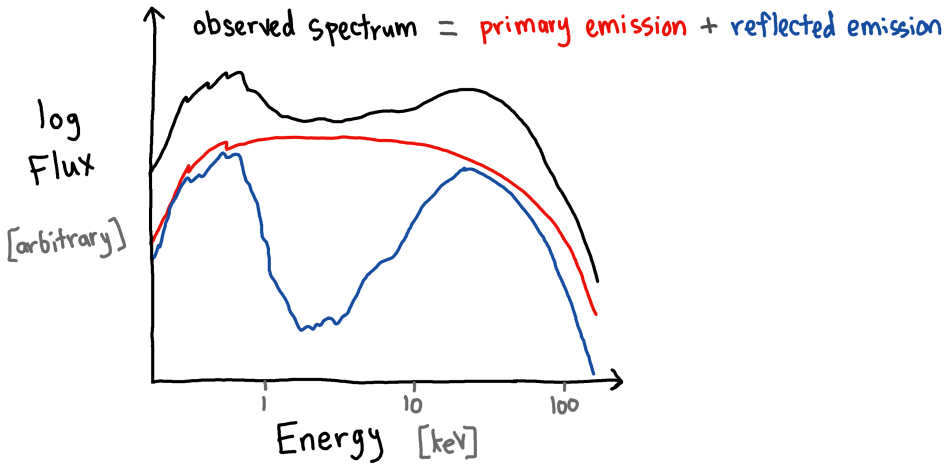

Figure 1.4: The observed X-ray spectrum of an AGN is a combination of the primary emission (a power-law) and the reflected emission. (Reproduced from Gallo 2011.)

disc are imprinted onto the reflected X-ray spectrum due to fluorescence. That is, when the primary emission strikes atoms in the disc they become ionised, releasing photons as higher-level electrons transfer to lower energy levels. Since iron has high fluorescent yield comsic abundances, it is this element which is most apparent in reflection spectra given current instrument resolutions. Doppler broadening occurs as a result of the rotation of the accretion disc. An intrinsically narrow emission line in a rotating disc will have a double-peaked profile due to the velocity distribution of material in the disc moving toward and away from the observer. These peaks will appear asymmetric due to special relativistic effects as light moving towards us is beamed and light moving away appears dimmer. An emission line will appear 'blurred' as photons escaping the gravitational potential well of the black hole lose energy and become redshifted.

The spectrum that we observe when we look at AGN is a combination of the primary X-ray emission from the corona and the reflected spectrum off the disc (Figure 1.4). By modelling this spectrum we can discern physical parameters of these components as well as any other components that might be present in the region.

1.3.3 The Nature of the Soft Excess

The 'soft excess' is a prominent feature of most Seyfert 1 spectra. As described in Section 1.3.2, the corona (the primary X-ray emitter) produces a spectrum of X-rays that takes the shape of a power-law. However, as shown in Figure 1.5, if we fit an observed spectrum with a power-law from $2 - 10$ keV and extrapolate that fit down to lower energies, we find that the power-law greatly underestimates the data at energies less than ~ 2 keV. This emission

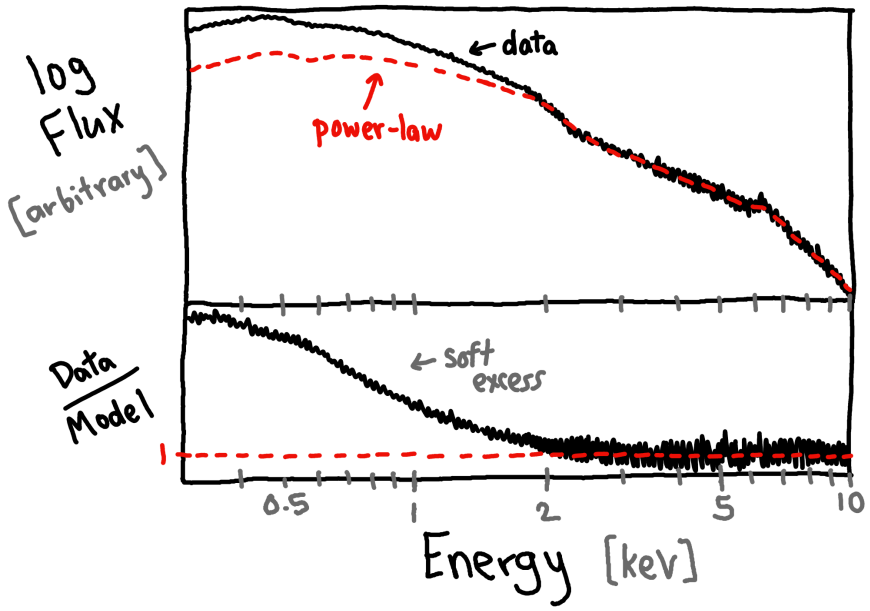

Figure 1.5: *Top panel:* Typical AGN X-ray spectrum (black) fit with a power-law (red) from $2-10$ keV and extrapolated down to 0.3 keV. *Bottom panel:* Ratio residuals of this fit, showing a strong soft excess below ~ 2 keV where the data deviates significantly from a power-law. (Reproduced from Mallick et al. 2017.)

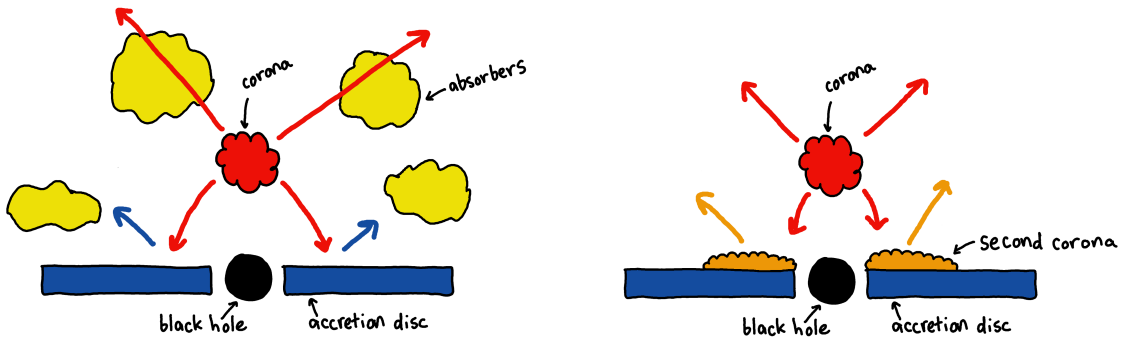

Figure 1.6: Schematics of possible scenarios responsible for producing the soft excess. *Left:* Absorption scenario. *Right:* Second corona scenario.

at low energies that is not described by a power-law is known as the soft excess of AGN. It indicates that there is an additional component (or components) beyond that of the corona. In Section 1.3.2 we showed that the soft excess could be described by the blurred reflector model (Figure 1.3, 1.4). However, other interpretations exist and determining the nature of this soft excess is a popular facet of X-ray studies of AGN. Thermal radiation from the accretion disc is not the cause of this excess, as the disc is not hot enough to produce emission at these energies. As hinted in Section 1.3.2, reflection of the primary emission off of the inner accretion disc could be responsible for this soft excess (e.g. Fabian et al. 1989; Laor 1991). Other possibilities include absorption (e.g. Gierliński & Done 2004; Tanaka et al. 2004) or a secondary corona (Magdziarz et al. 1998). If there are absorbing clouds of gas and dust in the central region around the black hole, they could absorb emissions from the corona, altering the shape of the spectrum (Figure 1.6, left panel). A second X-ray corona (Figure 1.6, right panel) could also produce the soft excess if it is cooler and more optically thick than the primary corona. It is likely that the mechanism (or mechanisms) producing the soft excess is variable between different AGN, or even at different times in the same AGN.

1.3.4 Variability

AGN are continuous emitters: rather than emitting in short bursts like many energetic astrophysical sources (e.g. supernovae, gamma-ray bursts), their emission is continuous over extended periods of time due to the continuous nature of the accretion process. Though AGN are continuously accreting and continuously emitting, the *rate* of accretion and emission is

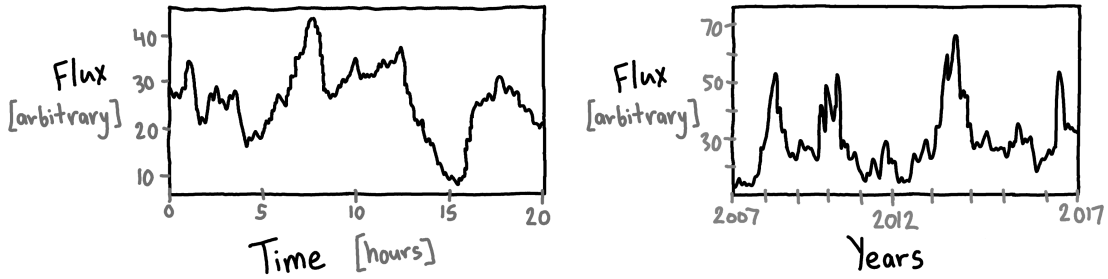

Figure 1.7: *Left:* Sample X-ray light curve of an AGN showing short timescale variability. *Right:* Sample X-ray light curve of an AGN showing long timescale variability. (Reproduced from Wilkins 2016.)

not constant; AGN emission is extremely variable on all observable timescales, and across all wavelengths. The shorter the wavelength of the emission, the shorter the timescale that it varies on; for example, X-rays vary on short timescales of minutes to hours (Figure 1.7, left panel). Such rapid variability in an object up to 10^9 $M_\odot$ is a remarkable and unique feature of AGN. Over the course of mere hours, X-ray flux in AGN can vary by orders of magnitude and sources can transition between high and low flux states.

X-ray flux is also variable on long timescales (Figure 1.7, right panel). Over extended periods of time, the X-ray flux emitted by AGN can vary by orders of magnitude. We have only been observing AGN for a few decades but in this time individual sources have exhibited strong variability at all wavelengths.

AGN variability can be caused by changes in any number of the central AGN components discussed in Section 1.3.2. Understanding the nature of this variability is paramount to understanding the physics and processes of the innermost black hole region and the mechanisms powering some of the most energetic sources in the Universe.

1.4 This Work

In this work we use X-ray observations of two AGN to study the X-ray emitting region. In Chapter 2 we look at Markarian 530. It is a Seyfert 1.5 AGN that has shown significant variability in optical spectra but has been poorly studied in the X-ray. It exhibits a strong soft excess which we attempt to characterise using spectral modelling to compare three scenarios: blurred reflection, partial covering, and soft Comptonisation. We also investigate a possible periodicity in the object. In Chapter 3 we look at Markarian 335, a well-studied and very bright Seyfert 1 that exhibits extreme variability. We build on prior works and test existing models in an attempt to characterise the variability using timing information. In Chapter 4 we summarize and conclude.

Chapter 2

Exploring the spectral variability of the Seyfert 1.5 galaxy Markarian 530 with *Suzaku*

Note: This chapter was published August 2018 in *Monthly Notices of the Royal Astronomical Society*, Volume 478, Issue 3, p.4214-4224, in collaboration with A.G. Gonzalez and L.C. Gallo.[1]

2.1 Introduction

Active galactic nuclei (AGN) harbour supermassive black holes (SMBHs) at their centres surrounded by an accretion disc and dusty torus, with both being illuminated by some central

[1]DOI: https://doi.org/10.1093/mnras/sty1306

X-ray source. AGN are responsible for producing extreme environments and are some of most luminous astrophysical sources in the Universe. The classification of these objects dates back to Seyfert (1943). At present the AGN unification model postulates that AGN classification depends primarily on viewing angle of the centre-most region (Antonucci 1993; Urry & Padovani 1995; Netzer 2015). For example, Seyfert 1 galaxies offer a relatively clean and unobstructed view of the central engine whereas Seyfert 2 galaxies are characterised by highly absorbed spectra due to our viewing angle intersecting the dusty, optically thick torus. A number of classifications between these extremes exist describing sources displaying characteristics akin to both Seyfert 1 and 2 type objects. These sources are classified as intermediate-type Seyferts (e.g. Seyfert 1.2, 1.5, 1.8).

Common to the basic unification model of AGN are the sites of X-ray emission that contribute to the overall shape of their X-ray spectrum, though these components are most easily studied in Seyfert 1 type objects due to the lack of strong absorption. Studies of such sources have revealed the primary X-ray emission source to be a hot, optically thin cloud of electrons (e.g. corona) that resides somewhere near the black hole, likely at some height above the accretion disc. The exact location and shape of this corona is a field of ongoing research and possible configurations investigated include point-like sources (e.g. Wilkins & Fabian 2012), as well as extended (e.g. Gonzalez et al. 2017), collimated (e.g. Wilkins & Gallo 2015a; Gonzalez et al. 2017), and patchy (e.g. Wilkins & Gallo 2015b) structures. The X-ray emission from this corona takes the form of a power law with photon index $\Gamma \sim 1.8$ roughly describing most AGN spectra. However, in most sources a simple power law fit to the spectrum is insufficient to describe the spectral shape and a soft excess below ~ 1 keV

is often observed.

The soft excess component may be the result of relativistic reflection off of the inner accretion disc (e.g. Fabian et al. 1989; George & Fabian 1991; Ross & Fabian 2005). X-ray emission from the hot corona will go on to illuminate both the accretion disc and dusty torus, producing a reflection spectrum for each component.

The reflection from the dusty torus shows the material to be neutral (cold) and distant matter as evidenced by the narrow and neutral Fe Kα emission lines. Reflection off the inner accretion disc, however, leads to relativistically broadened emission features due to the general relativistic effects experienced by the material being strongly affected by the gravitational field of the black hole (e.g. Fabian et al. 1989; Laor 1991). The forest of emission lines in the < 1 keV band will thus become broadened and blurred into a smooth, featureless hump, therefore accounting for the soft excess component.

An alternative explanation to this soft excess describes a second X-ray corona comprising the innermost region of the accretion disc (Magdziarz et al. 1998). Here the cooler, more optically thick corona acts as a site for soft Comptonisation of seed UV photons from the accretion disc. In this scenario the soft excess is accounted for by this soft Comptonising corona with the power law emission resulting from the hot, optically thin corona above the disc.

In addition to both of these explanations for the soft excess it is also possible that in systems being observed at higher inclinations absorption effects could produce similarly shaped spectra (e.g. Gierliński & Done 2004; Tanaka et al. 2004). The existence of gas and dust clouds in the central region of AGN may act to partially obscure the view of the

centre-most region. These smaller clouds of matter can therefore greatly affect the spectral shape and variability in AGN. These partial covering absorbers may mimic the signatures of relativistic reflection and soft Comptonisation via the absorption of intermediate-energy X-rays such that a soft excess is produced.

Seyfert galaxies exhibit many types of variability over various timescales (e.g. Grupe et al. 2012). Periodic behaviour, though commonly detected in X-ray binaries, is something of a rarity for AGN (Zhang et al. 2018) with only a handful of objects exhibiting evidence of periodicity in the X-ray. Some examples include RE J1034+396 (Gierliński et al. 2008), 1H 0707−495 (Pan et al. 2016), Mrk 766 (Zhang et al. 2017), and NGC 3516 (Iwasawa et al. 2004). Power spectrum analyses of these sources revealed periodic variability in a narrow band simultaneous with broadband variability, with the exception of NGC 3516 which exhibited only a few periods of sinusoid-like behaviour in the light curve.

There has been much debate over the significance of the detected periods in AGN, as a number of claims of periodicity in such objects have been disproved (e.g. Madejski et al. 1993; Barth & Stern 2018). The robust measurements are often associated with quasi-periodic oscillations (QPOs) in a broad continuum band or modulations in the relativistic broadened Fe Kα emission line.

Markarian 530 (NGC 7603, $z = 0.0295$; hereafter Mrk 530) is a bright (flux in $2-10$ keV band of $\sim 2 \times 10^{-11}$ ergs cm^{-2} s^{-1}) Seyfert 1.5 galaxy that has been included in numerous surveys studying various wavelength regimes (e.g. Lal et al. 2004; Singh et al. 2013; Theios et al. 2016; Malkan et al. 2017). Mrk 530 has a line-of-sight companion galaxy (NGC 7603B) that is at a higher redshift and connected by filaments observed in optical (e.g. López-

Corredoira & Gutiérrez 2002). Features of possible tidal origin surrounding Mrk 530 have been identified in optical images, indicating that the galaxy may have undergone a recent merger event (Slavcheva-Mihova & Mihov 2011). Mrk 530 has been found to be a so-called "changing-look" AGN (e.g. Matt et al. 2003; Puccetti et al. 2007; LaMassa et al. 2015) as it apparently changes from a Seyfert type 1.9 to type 1.0 (Goodrich 1995; Mickaelian 2016). The object has shown optical spectral variations over the course of months to years and exhibits stronger amplitudes of optical emission line variability compared to other Seyferts (Kollatschny et al. 2000). Mrk 530 remains relatively poorly studied with modern X-ray telescopes. This work presents an in-depth X-ray spectral analysis of Mrk 530 with *Suzaku*.

The work presented here is organised in the following manner. In Section 2.2 we list the observations of Mrk 530 that we analysed as well as the methods used in the analysis. Section 2.3 presents the timing variability observed and a brief look into the spectral variability. Initial spectral fits are performed in Section 2.4. The spectral modelling for the average, soft and hard, and phase-resolved spectra are presented in Sections 2.5, 2.6, and 2.7, respectively. We discuss the results more in-depth in Section 2.8 and finally conclude in Section 2.9.

2.2 Observations & Data Reduction

Mrk 530 was observed with the *Suzaku* satellite starting 6 June 2012 (observation ID 707003010) in the XIS-nominal position for a total exposure time of $\sim$ 101 ks. Data were collected by the two front-illuminated (FI) CCDs (XIS0 and XIS3), the back-illuminated (BI) CCD (XIS1) and the HXD-PIN detectors. The XSELECT software was used to extract spectra and light curves from the XIS detector event list files. Source spectra were extracted from a circular region centred on the source with a radius of $4'$ and background spectra were selected from a circular region off-source with a $2'$ radius. The RMF response matrices and ARF ancillary response files for the observations were generated using XISRMFGEN and XISSIMARFGEN, respectively. Spectra from XIS0 and XIS3 were merged using ADDASCASPEC after ensuring that the spectra were consistent. The XIS1 data were also checked for consistency though these were not used in this analysis for the sake of simplicity. These were omitted in order to avoid inconsistencies arising from cross-calibration of the FI- and BI-CCD detectors. We favour use of the FI-CCDs due to the higher number of counts available from merging the spectra of XIS0 and XIS3.

Source and background spectra from the HXD-PIN detector were extracted using HXDPINXBPI. The source is detected up to 30 keV.

2.3 Light Curves & Hardness Ratio

The broadband ($0.3-10$ keV) light curve of Mrk 530 taken by the XIS0+3 detectors is shown in the top panel of Figure 2.1. The weighted average count rate is 3.561 ± 0.006 counts s^{-1} as indicated by the dashed grey line in the panel. A constant fit to the light curve yields a poor fit with a statistic of $\chi^2_\nu = 12.65$, indicating moderate short-term variability. The fractional variability (Edelson et al. 2002) of the broadband light curve is 3.4 ± 0.5 per cent.

The broadband light curve shows a curious sinusoidal behavior, displaying two clear peaks and troughs of roughly the same amplitude. However, red noise can often mimic a few cycles of sinusoidal behaviour (Vaughan et al. 2016), and so robust detections of QPO behaviour have been those that have been detected in addition to the broadband aperiodic variability. Nonetheless, to characterise the light curve, a sine function of the form:

$$y = A \sin(\omega x + \phi) + c \tag{2.1}$$

was fit to the broadband light curve with A, ω, ϕ, c as free parameters. This fit, plotted as the red curve in the top panel of Figure 2.1, yielded a statistic of $\chi^2_\nu = 2.57$ and a period of $T \approx 86$ ks.

To investigate spectral variability, light curves were made in three different energy bands. The $0.5 - 1$ keV, $1 - 3$ keV, and $3 - 10$ keV energy ranges were chosen to represent the soft excess, continuum emission, and hard emission, respectively. These light curves are shown in the second, third, and fourth panels of Figure 2.1. The red curve plotted over each light curve is Equation 2.1 fit to the broadband light curve and renormalised to the average

count rate of the light curve on which it is plotted. This reveals that the seemingly periodic variability is primarily seen in the intermediate energy band between $1 - 3$ keV.

To further characterise the oscillatory variability of this observation, phase-resolved spectra were created by dividing the broadband light curve into the segments denoted by vertical lines in the top panel of Figure 2.1 labelled A, B, C, D, E. These segments were chosen such that each spectrum corresponded to either a peak (B, D) or trough (A, C, E) in the light curve, and the segments were relatively equally-spaced.

The bottom panel of Figure 2.1 shows the hardness ratio (HR) of the $2 - 10$ keV (hard) band count rate divided by the $0.5 - 1$ keV (soft) band count rate. The weighted average of the hardness ratio is 2.40 ± 0.01 as indicated by the dashed grey line in the panel. The weighted average fit to the hardness ratio produces a fit statistic of $\chi^2_\nu = 10.23$ indicating significant changes in the hardness ratio over the course of the observation. Examining the shape of the hardness ratio reveals two distinct spectral states: a soft state (HR < 2.4 and $t \lesssim 50$ ks) which then transitions to a hard state (HR > 2.4 and $t \gtrsim 50$ ks). This transition is remarkably smooth and gradual over time. It should be noted that the designation of soft and hard states in this analysis should not be interpreted as major changes in the accretion geometry associated with major changes in the Eddington rate as in BH X-ray binaries; this is merely a distinction of the different intervals observed in the hardness ratio.

Time segment A of the hardness ratio is entirely in the soft state, segment B the transition state, and segments C, D, E are entirely in the hard state. These segments are divided by the blue vertical lines in the panel, which correspond to the segments labelled in the top panel of the figure.

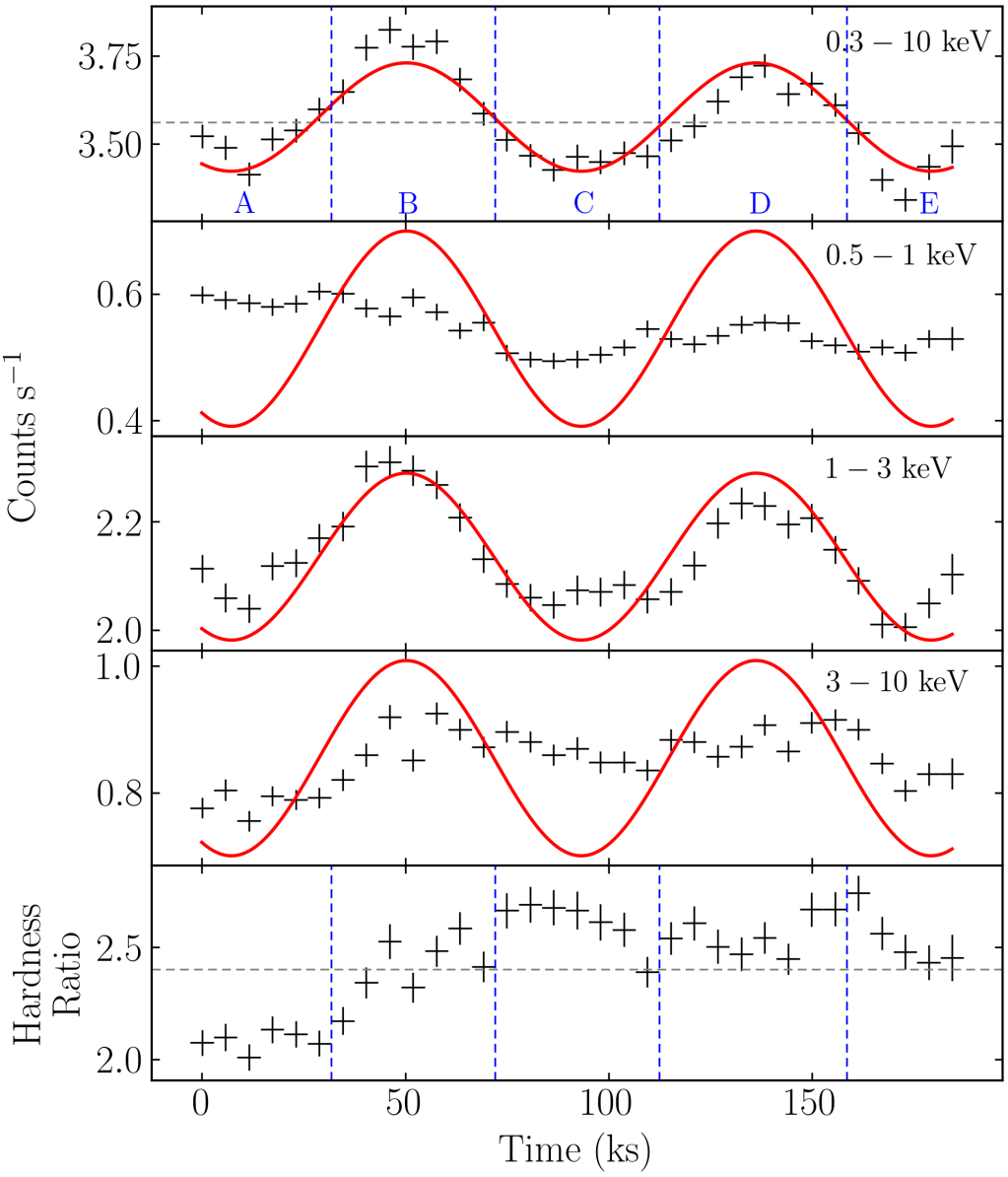

Figure 2.1: *Top panel:* Broadband (0.3 – 10 keV) light curve from the FI-XIS detectors fit with a sine curve. Horizontal line indicates weighted mean count rate. Vertical lines denote divisions used to create phase-resolved spectra. *Middle panels:* Light curves of the 0.5 – 1 keV, 1 – 3 keV, and 3 – 10 keV bands with the same sine function overplotted, renormalised to the average count rate of each light curve. *Bottom panel:* Hardness ratio (hard/soft) between the 0.5 – 1 keV (soft) and 2 – 10 keV (hard) energy bands. Horizontal line indicates weighted mean hardness ratio. Vertical lines denote phase-resolved segments (A,B,C,D,E) as in top panel.

2.4 Initial Spectral Fits

2.4.1 General

XIS0+3 data were optimally binned as described by Kaastra & Bleeker (2016) using the PYTHON code written by C. Ferrigno[2]. Due to instrument calibration and sensitivity, energy channels below 0.7 keV and above 10 keV were omitted from the XIS0+3 data. Additionally, the energies $1.72 - 1.88$ keV and $2.19 - 2.37$ keV were omitted due to known instrument calibration issues (Nowak et al. 2011). PIN data within the energy range of $15 - 30$ keV were also used in this analysis, though they were not binned due to insufficient counts.

The X-ray spectral modelling software XSPEC v.12.9.1 (Arnaud 1996) was used to perform all spectral fitting. Fit quality was quantified in XSPEC using the C-statistic, a modification of the Cash statistic (Cash 1979), which has been been shown to be an appropriate statistic for X-ray astronomy (e.g. Humphrey et al. 2009; Mantz et al. 2017). The Galactic column density toward Mrk 530 was kept frozen at 3.82×10^{20} cm^{-2} (Kalberla et al. 2005) during all spectral fitting. The cross-normalisation factor between the XIS and HXD-PIN detectors during this observation was frozen to 1.16 as the observation of Mrk 530 was taken in the XIS nominal position[3]. All errors are calculated to a 90 per cent confidence level.

2.4.2 Simple Models

The broadband data that were used in spectral fitting are shown in the top panel of Figure 2.2. To examine the spectrum, we first fit it with a power-law (model PO in XSPEC) account-

[2] `https://cms.unige.ch/isdc/ferrigno/developed-code/`

[3] From section 5.5.11 of Suzaku Data Reduction Guide: `https://heasarc.gsfc.nasa.gov/docs/suzaku/analysis/abc/node8.html`

ing for Galactic absorbtion along our line of sight (TBABS; Wilms et al. 2000). This model (TBABS*PO) was fit from $2-10$ keV to model the continuum emission, and then extrapolated to lower and higher energies to cover the full extent of the XIS and PIN detectors. The ratio residuals (data/model) of this fit are shown in the middle panel of Figure 2.2. This reveals a strong soft excess present in Mrk 530 below 2 keV, as well as a weak excess between $8-15$ keV and excess emission in the Fe Kα band.

To model this soft excess we first used the simplest model, in which the soft excess is described by thermal blackbody radiation from the accretion disc. We included in this model a single redshifted Gaussian emission line that was left free to vary in both energy and width. The model (CONST*TBABS*(PO+BB+ZGAUSS) in XSPEC) was fit to the broadband data, yielding the ratio residuals shown in the bottom panel of Figure 2.2. This fit, with a statistic of C/d.o.f. = 190/166, produced a broadened emission line at ~ 6.4 keV with a width of $\sigma \sim 85$ eV. The fit yielded a blackbody temperature of 380 ± 30 eV, which rules out this model as physically realistic, as the temperature is too high to originate from the accretion disc.

To characterise the data and the nature of the soft excess, we explored three different physical models: a blurred reflection model (Section 2.5.1), a partial covering model (Section 2.5.2), and a soft Comptonisation model (Section 2.5.3).

2.4.3 The Fe Kα band

Fitting the $2-10$ keV spectrum with only an absorbed power-law leaves strong residuals in the Fe Kα region (around $6-7$ keV) (Figure 2.3, top panel). Though fit from $2-10$

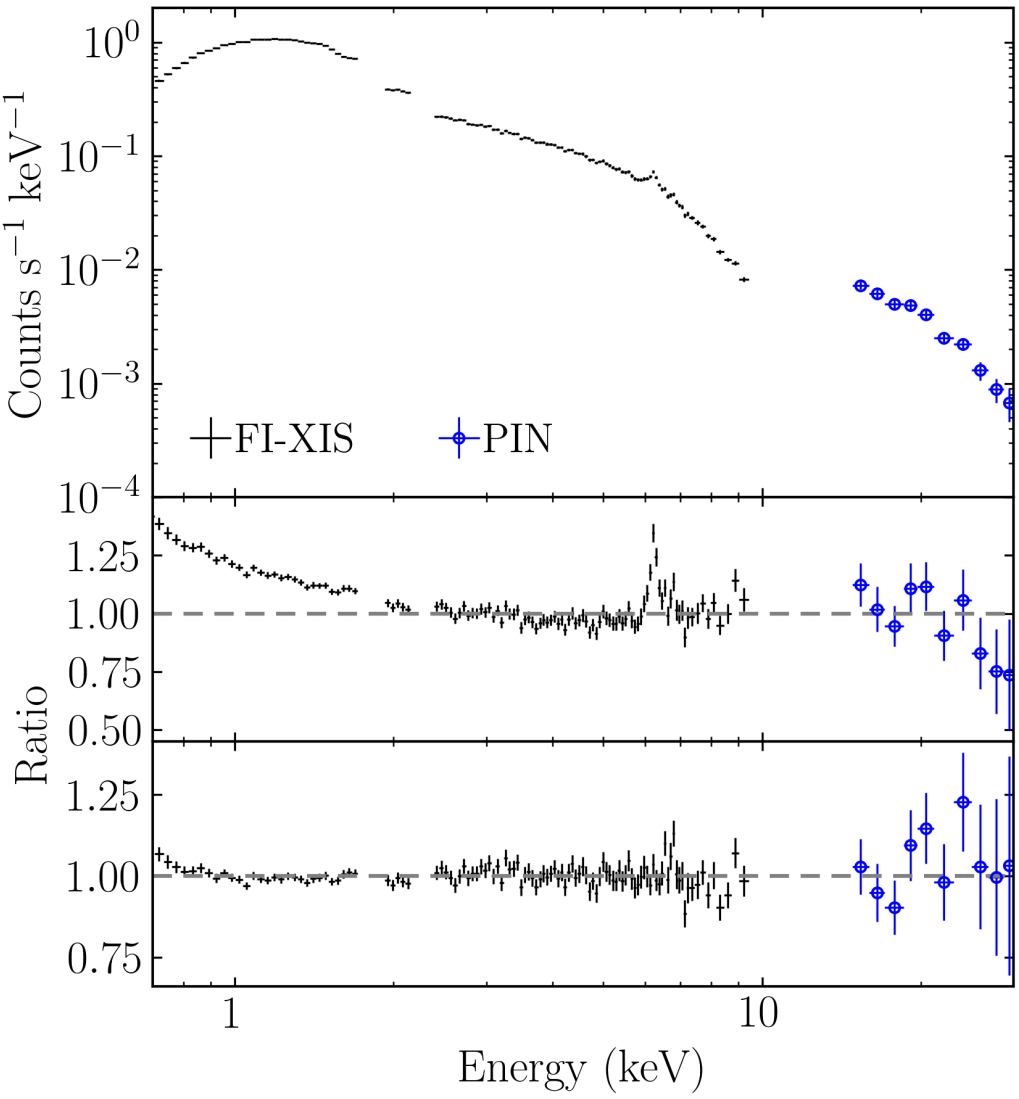

Figure 2.2: *Top panel:* Spectrum of *Suzaku* observation of Mrk 530 used in this analysis. *Middle panel:* Ratio residuals of an absorbed power-law model fit from $2-10$ keV and extrapolated over $0.7-30$ keV, showing a strong soft excess below 2 keV and strong curvature between $8-15$ keV, as well as residuals in the Fe Kα band. *Bottom panel:* Ratio residuals of a blackbody model with a broad Gaussian fit to the broadband spectrum.

keV, this figure displays only the $5-8$ keV band to clearly see changes in the Fe Kα region. This fit exhibits strong residuals in this region and yields a poor fit with a statistic of C/d.o.f. = 328/101.

As shown in the bottom panel of Figure 2.2, a single broad Gaussian is unable to account for the residuals in the Fe Kα region. We thus consider a multiple narrow-line scenario. First, a narrow emission line was added to the absorbed power-law model (TBABS*(PO+ZGAUSS)) at an intrinsic line energy of 6.4 keV. This line, corresponding to the Kα emission lines from neutral (or low ionized) iron (Fe I Kα), was fixed to a width of $\sigma = 1$ eV, as were all narrow lines. This Gaussian component improved the fit, yielding C/d.o.f. = 170/100. The ratio residuals of this fit are shown in the second panel of Figure 2.3. The excess residuals exist blueward of 6.4 keV, which may not be fully consistent with relativistic blurring. To further improve the residuals, a second narrow Gaussian feature was fit to an intrinsic energy of 6.7 keV. The ratio residuals of this fit are shown in the third panel of Figure 2.3. This line corresponds to a Kα emission line from He-like iron (Fe XXV Kα). This additional component betters the fit, yielding C/d.o.f. = 153/99. A narrow Gaussian line was then fit to an intrinsic energy of 6.97 keV, which corresponds to a Kα emission line from H-like iron (Fe XXVI Kα). This fit, the ratio residuals of which are shown in the fourth panel of Figure 2.3, further improved the fit, yielding a statistic of C/d.o.f. = 132/98. Vertical lines in Figure 2.3 denote the observed energies at which these Gaussian profiles were fit. We modelled the Compton shoulder with a Gaussian at an intrinsic energy of 6.3 keV and fixed to a normalisation one tenth that of the Fe I Kα line (Matt et al. 1991). However, while the data were consistent with this, this addition did not significantly improve the fit

(C/d.o.f = 131.69/98). Additionally, it should be noted that a Gaussian at 6.3 keV is a crude approximation of the Compton shoulder.

The data can support an alternative interpretation to the single broad emission line and the multiple narrow line scenarios described above. Fitting a narrow line fixed at 6.4 keV with a width of $\sigma = 1$ eV and fitting a second Gaussian with energy and width left free to vary produces a broad line at 6.7 keV with a width of $\sigma = 400 \pm 200$ eV. This fit, with a statistic of C/d.o.f. = 134/97, can also reasonably account for the Fe Kα excess. The ratio residuals of this fit are shown in the bottom panel of Figure 2.3.

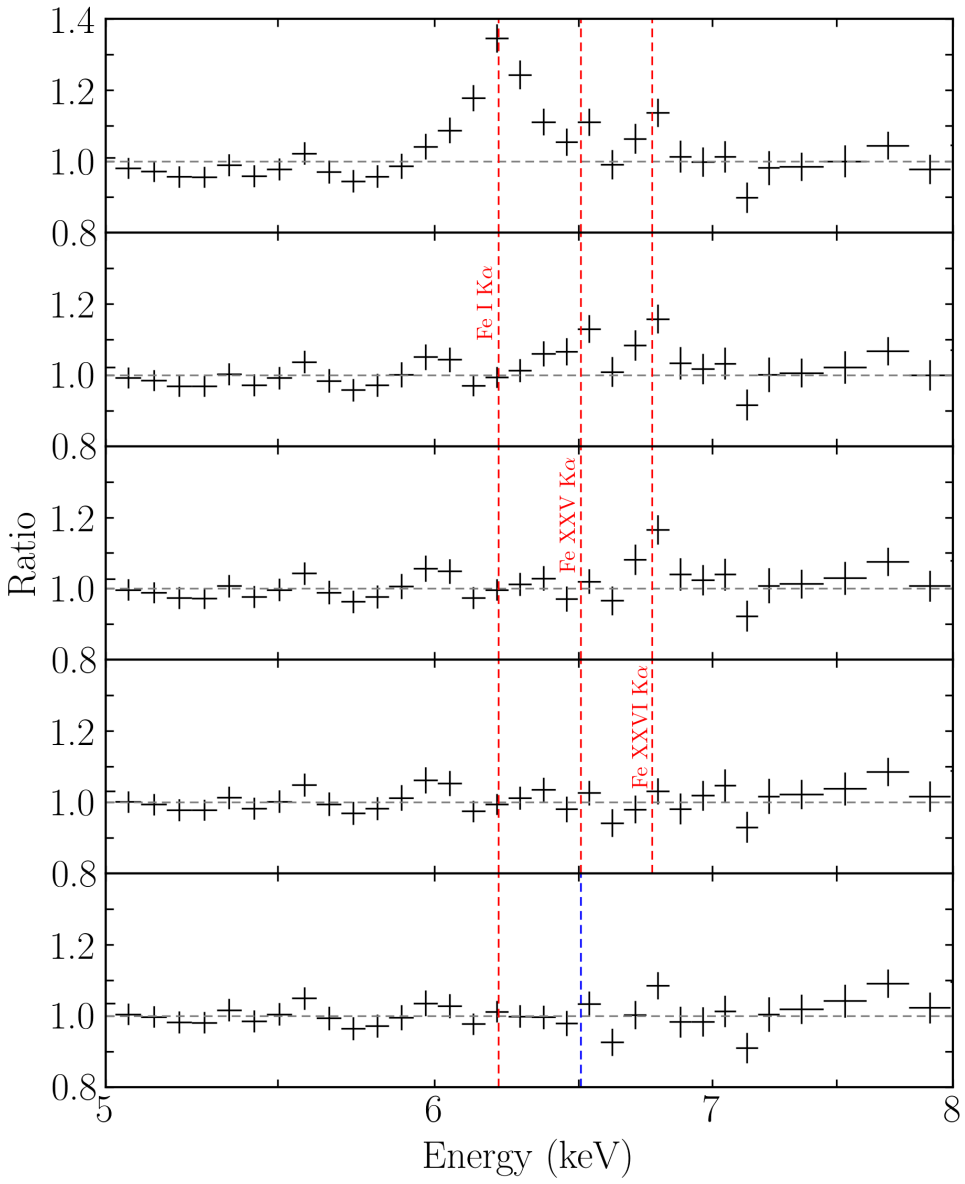

Figure 2.3: *Top panel:* Ratio residuals of the $2-10$ keV region fit with absorbed power-law. *Top-middle panel:* As above, but model includes a narrow Gaussian line fixed at 6.4 keV to fit the Fe I Kα emission line. *Middle panel:* As above, with another Gaussian line at 6.7 keV to fit the Fe XXV Kα emission line. *Bottom-middle panel:* As above, with a narrow Gaussian line at 6.97 keV to fit the Fe XXVI Kα emission line. *Bottom panel*: Ratio residuals of the $2-10$ keV region fit absorbed power-law with narrow Gaussian at 6.4 keV and a broad Gaussian at 6.7 keV. Vertical dashed lines indicate observed energies to which these lines were fit.

2.5 Physical Models

2.5.1 Blurred reflection

The curvature present in the average broadband spectrum of Mrk 530 may be interpreted in a number of ways. One scenario that can account for the shape is relativistic reflection off of the inner region of the accretion disc. We therefore begin by fitting the average broadband X-ray spectrum with blurred ionised reflection (RELXILL, García et al. 2014; Dauser et al. 2014).

The fit parameters are shown in Table 2.1. The model consists of a cut-off power law, blurred ionised reflector, and neutral reflector; in XSPEC the model is: CONST*TBABS*(CFLUX*CUTOFFPL+CONST*CFLUX*RELXILL+PEXMON+ZGAUSS+ZGAUSS). The cut-off energy of the power-law component was frozen to $E_{\rm cut} = 300$ keV as the fit was unable to constrain it when allowed to vary. We have assumed the black hole spin parameter is maximal, therefore allowing the inner radius of the accretion disc to extend to the minimum allowed by the model. The disc is assumed to be illuminated such that emissivity index is constant at $q = 3$ over the entire disc. Allowing these parameters to vary freely found them to be poorly constrained, thus they are frozen at the listed values. Iron abundance in the accretion disc was found to be consistent with solar and therefore it is frozen at $A_{\rm Fe} = 1.0$. The use of CFLUX allows for the flux of the power law and reflection components to be set equal, letting the modulation of the flux from the blurred reflection component to be computed external to the model with a simple constant component.

Reflection from the cold distant torus was modelled using PEXMON (Nandra et al. 2007).

This model includes neutral Compton reflection and self-consistent Fe and Ni emission lines, including the 6.4 keV Fe Kα emission line and the Compton shoulder. Two additional Gaussian components were added to this model to account for the ionised iron emission lines at 6.7 keV and 6.97 keV. The model components are shown in the top left panel of Figure 2.4.

The ratio residuals of the blurred reflection model fit to the average spectrum are shown in the bottom left panel of Figure 2.4. The fit is of good statistical quality, with C/d.o.f. = 171/166. This model describes a scenario in which a moderately steep power law illuminates the accretion disc and torus. The accretion disc emission is highly ionised and is a significantly weaker component than the power-law, as the reflection fraction is low ($R = 0.22$). The inclusion of the cold distant reflection component is necessary to model the high energy curvature in the spectrum. However, even with the inclusion of both reflection components the ratio residuals above ~ 8 keV deviate significantly from the model, indicating further curvature in the spectrum.

2.5.2 Partial covering

An alternate explanation to the curvature observed in the average spectrum of Mrk 530 is partial covering of the inner region by ionised and/or neutral clouds obscuring the system. The partial covering absorption was modelled by using the XSPEC model ZXIPCF. The fit parameters for such a scenario are given in Table 2.1. The model consists of two partial covering absorbers convolved with a cut-off power-law as well as a neutral reflection component; the XSPEC model is: CONST*TBABS*(ZXIPCF*ZXIPCF*CFLUX*CUTOFFPL+PEXMON+

ZGAUSS+ZGAUSS). During the fitting procedure it was found that only one absorber required ionisation to be left free while the other was consistent with neutral material. The neutral material was modelled by freezing the ionisation parameter ($\xi = 4\pi F/n$, where F is the flux of the illuminating radiation and n the gas density) to $\log \xi = -3$, the minimum allowed by the model. Here CFLUX is used to give the unabsorbed flux of the power-law. The Gaussian components are again added to fit the 6.7 keV and 6.97 keV emission features. The model components are shown in the top centre panel of Figure 2.4.

The data are over-fit by this absorption model, with C/d.o.f. = 144/163. The ratio residuals, shown in the bottom centre panel of Figure 2.4, reveal that the high-energy curvature is minimised with this model, though at the lowest energies ($\lesssim 0.9$ keV) deviations from the model can be seen. This is likely indicative of a stronger soft excess than is predicted by the model. The lack of sensitivity below 0.7 keV in *Suzaku* makes it difficult to investigate further.

In this scenario a neutral, high column-density cloud partially obscures a large amount of the power-law emission while a lightly ionised, lower column-density cloud partially obscures less of the emission. The power-law itself is much steeper than in the blurred reflection case and the cold reflection component is also brighter by a factor of two.

2.5.3 Soft Comptonisation

The curvature in the spectrum of Mrk 530 can also be described by a soft Comptonisation scenario (e.g. Matt et al. 2014), which was modelled with OPTXAGNF (Done et al. 2012). This model describes the soft excess with a thermal Comptonisation disc component that is

optically thick with a low temperature, and models the continuum emission above 2 keV with an optically thick, high temperature thermal Comptonisation. The torus was again modelled with PEXMON and the two ionised iron emission lines were included. The broadband continuum was modelled by CONST*TBABS*(OPTXAGNF+PEXMON+ZGAUSS+ZGAUSS), the fit parameters of which are shown in Table 2.1. Figure 2.4 displays the model components (upper right panel) and fit ratio residuals (bottom right panel).

During the fit, the following five OPTXAGNF parameters were left free to vary: the Eddington ratio ($L/L_{\rm edd}$), electron temperature in the soft component (kT_e), optical depth of soft component (τ), photon index of hard component (Γ), and fraction of the power in the hard component ($f_{\rm pl}$). Black hole spin was frozen to the maximum value as a range of values for spin were implemented and that was found to produce the best fit. The coronal radius r_{cor} was fixed to 10 r_g as the Eddington ratio was found to be insensitive to radii less than that. The Eddington ratio was found to become lower with increasing $r_{\rm cor}$ until about 10 r_g, at which point the Eddington ratio became insensitive to the parameter. Since Singh et al. (2011) found an Eddington ratio for Mrk 530 of $\log(L/L_{\rm edd}) = -2.06$ which was much lower than this model would allow, we thus froze $r_{\rm cor}$ to the value which minimized the Eddington ratio. The radius of the outer disc was frozen to 1000 r_g as the fit was insensitive to this parameter. The cutoff energy of the PEXMON model was fixed to 300 keV for consistency between the three compared models.

This soft Comptonisation model over-fits the data with C/d.o.f = 160/165. The same trend is observed in these residuals as those from the partial covering model: the high-energy curvature is minimised, but there remains a soft excess at the lowest observable energies.

Table 2.1: Parameter values for the three models fit to the average spectrum (FI-XIS & PIN) for Mrk 530. All values without uncertainties are frozen during the fitting, as allowing them to be free did not improve the fit significantly. ZGAUSS norm in units of source frame photons cm^{-2} s^{-1}. PEXMON norm in units of observed frame photons keV^{-1} cm^{-2} s^{-1} at 1 keV of the cutoff power-law. CFLUX norm in units of source frame photons keV^{-1} cm^{-2} s^{-1} at 1 keV.

Model	Parameter	Blurred Reflection	Partial Covering	Soft Comptonisation
CFLUX	$E_{\rm min}$ [keV]	0.1	0.1	–
	$E_{\rm max}$ [keV]	100	100	–
	$\log F$ [erg cm^{-2} s^{-1}]	$-10.08^{+0.02}_{-0.03}$	-9.72 ± 0.06	–
CUTOFFPL	Γ	1.97 ± 0.02	2.22 ± 0.06	–
	$E_{\rm cut}$ [keV]	300	300	–
	norm ($\times 10^{-2}$)	1	1	–
CONST	R	$0.22^{+0.08}_{-0.07}$	–	–
RELXILL	$q_{\rm in}$	3.0	–	–
	$q_{\rm out}$	3.0	–	–
	$R_{\rm break}$ r_g	15.0	–	–
	a	0.998	–	–
	i [°]	61.5 [a]	–	–
	$R_{\rm in}$ [r_g]	1.235	–	–
	$R_{\rm out}$ [r_g]	400	–	–
	Γ	1.97 *	–	–
	$\log \xi$ [erg cm s^{-1}]	2.8 ± 0.2	–	–
	$A_{\rm Fe}$	1.0	–	–
	$E_{\rm cut}$ [keV]	300	–	–
	$R_{\rm rel}$	-1	–	–
	norm	1	–	–
ZXIPCF	N_H ($\times 10^{22}$) [cm^{-2}]	–	22^{+7}_{-3}	–
	$\log \xi$ [erg cm s^{-1}]	–	-3	–
	CF	–	0.41 ± 0.05	–
ZXIPCF	N_H ($\times 10^{22}$) [cm^{-2}]	–	$1.9^{+0.8}_{-0.4}$	–
	$\log \xi$ [erg cm s^{-1}]	–	$-0.6^{+1.0}_{-0.4}$	–
	CF	–	$0.26^{+0.07}_{-0.05}$	–
OPTXAGNF	$M_{\rm BH}$ [$M_\odot$]	–	–	1.15×10^8 [b]
	D [Mpc]	–	–	118.3 [c]
	$\log L/L_{\rm Edd}$	–	–	$-1.74^{+0.03}_{-0.02}$
	a	–	–	0.998
	$r_{\rm cor}$ [r_g]	–	–	10
	$r_{\rm out}$ [r_g]	–	–	1000
	$kT_{\rm e}$ [keV]	–	–	5.5 ± 1
	τ	–	–	5.75^{+4}_{-2}
	Γ	–	–	$2.22^{+0.11}_{-0.08}$ *

Continued on next page

Table 2.1 – *Continued from previous page*

Model	Parameter	Blurred Reflection	Partial Covering	Soft Comptonisation
	$f_{\rm pl}$	–	–	$0.83^{+0.09}_{-0.11}$
	k	–	–	1
PEXMON	Γ	1.97*	2.22*	2.22*
	$E_{\rm cut}$ [keV]	300	300	300
	$R_{\rm rel}$	-1	-1	-1
	A	1.0	1.0	1.0
	$A_{\rm Fe}$	1.0	1.0	1.0
	i [°]	61.5 [a]	61.5 [a]	61.5 [a]
	norm ($\times 10^{-3}$)	5.5 ± 0.9	10 ± 2	10^{+4}_{-2}
ZGAUSS	E [keV]	6.7	6.7	6.7
	σ [eV]	1	1	1
	norm ($\times 10^{-6}$)	4 ± 3	$< 4.9_p$	4 ± 3
	EW [eV]	14^{+11}_{-9}	8^{+10}_{-8}	14^{+10}_{-9}
ZGAUSS	E [keV]	6.97	6.97	6.97
	σ [eV]	1	1	1
	norm ($\times 10^{-6}$)	3 ± 3	$< 3.7_p$	3 ± 3
	EW [eV]	11 ± 10	4^{+13}_{-4}	12^{+10}_{-11}
Fit Quality	C/d.o.f.	171/166	144/163	160/165
		1.03	0.88	0.97

Note: Values with * are tied to power-law (CUTOFFPL). p denotes lower limit is pegged at zero.
References: (*a*) Monje et al. 2011 (*b*) Woo et al. 2012 (*c*) Lal et al. 2011

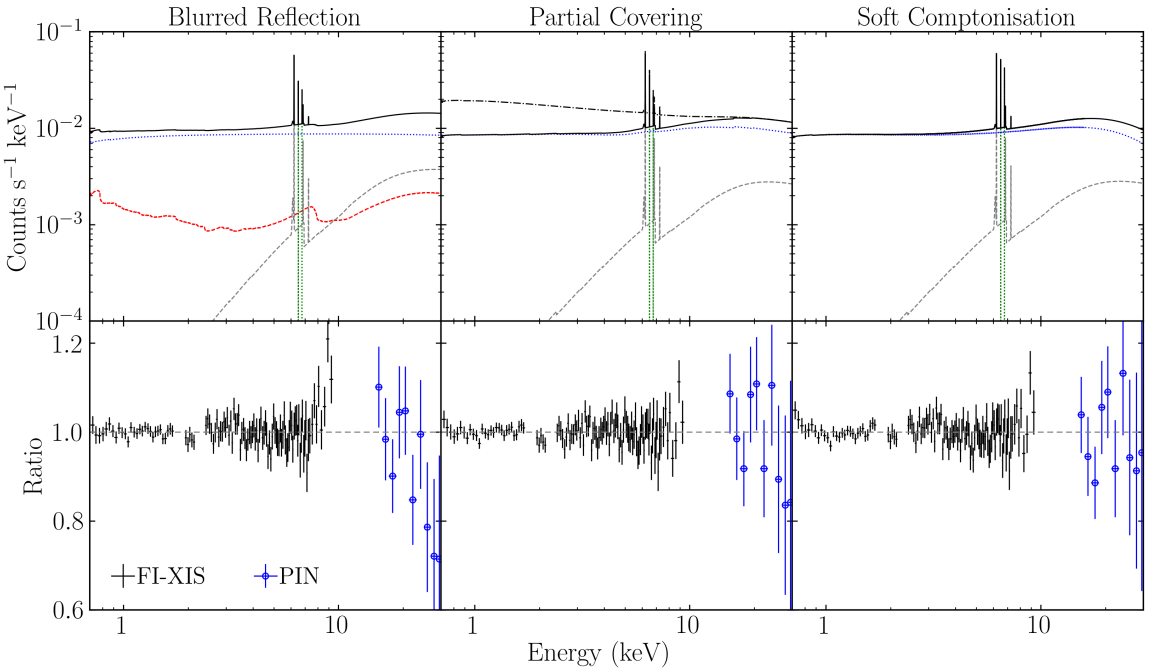

Figure 2.4: Models (top row) and ratio residuals (bottom row) of the three tested models: blurred reflection (left), partial covering (middle), and soft Comptonisation (right). Blurred reflection model components include power-law (blue), ionised iron lines (green), reflection from torus (grey), and reflection from accretion disc (red). Partial covering model components include absorbed power-law (blue), ionised iron lines (green), and reflection from torus (grey). Unabsorbed spectrum is shown by the black dot-dash curve. Soft Comptonisation model includes soft Comptonised power-law (blue), ionised iron lines (green), and reflection from torus (grey).

2.6 Soft to hard state spectral changes

As indicated by the hardness ratio in the bottom panel of Figure 2.1, there are two distinct spectral states present in this observation. Spectra were made of these two states, henceforth called the soft spectrum (which covers the same time range as segment A) and hard spectrum (which covers the time intervals C to E). Spectral fitting of the above three models was performed on these spectra in an effort to understand the driver of the variability between these spectral states. Section 2.6.1 contains the blurred reflection fits to the soft and hard states, Section 2.6.2 the partial covering fits, and Section 2.6.3 the soft Comptonisation fits.

2.6.1 Blurred reflection

The soft and hard spectra were fit with the same blurred reflection model as in Section 2.5.1, keeping all parameters frozen to the value obtained from fitting the average spectrum, with the exception of those listed in Table 2.2. The table shows the parameter values for those that were left free to vary between the soft and hard states, as well as the free parameters that were linked between the two states.

Notably, to account for the spectral change between soft and hard we require the photon index and reflection fraction free to vary between the states. This produces a good statistical fit of $C/\text{d.o.f.} = 292/285$ and the ratio residuals shown in the top panel of Figure 2.5. By simultaneously hardening the power law and decreasing the reflection fraction (i.e. reducing the soft band curvature) we are able to harden the overall spectrum, therefore explaining the spectral state change.

Table 2.2: Parameters obtained by fitting the soft and hard spectra of Mrk 530 with the three described models. A value in the middle of the column denotes a parameter that was linked between the two states.

		Blurred Reflection		Partial Covering		Soft Comptonisation	
Model	Parameter	Soft	Hard	Soft	Hard	Soft	Hard
CFLUX	$\log F_{0.1-100}$ [erg cm^{-2} s^{-1}]	$-10.12^{+0.01}_{-0.02}$		-9.74 ± 0.02		–	
CUTOFFPL	Γ	2.03 ± 0.02	$1.99^{+0.01}_{-0.02}$	2.27 ± 0.03		–	
CONST	R	$0.34^{+0.05}_{-0.04}$	$0.22^{+0.06}_{-0.05}$	–		–	
RELXILL	$\log \xi$ [erg cm s^{-1}]	2.7 ± 0.1		–		–	
ZXIPCF	$N_{\rm H}$ ($\times 10^{22}$) [cm^{-2}]	–		22^{f}		–	
	$\log \xi$ [erg cm s^{-1}]	–		-3^{f}		–	
	CF	–		0.41^{f}		–	
ZXIPCF	$N_{\rm H}$ ($\times 10^{22}$) [cm^{-2}]	–		1.9^{f}		–	
	$\log \xi$ [erg cm s^{-1}]	–		-0.6^{f}		–	
	CF	–		0.20 ± 0.04	0.29 ± 0.03	–	
OPTXAGNF	$\log L/L_{\rm Edd}$	–		–		-1.62 ± 0.04	-1.74 ± 0.01
	$kT_{\rm e}$ [keV]	–		–		7^{+2}_{-1}	
	τ	–		–		$4.8^{+0.8}_{-0.7}$	
	Γ	–		–		$2.43^{+0.07p}_{-0.08}$	$2.27^{+0.03}_{-0.04}$
	$f_{\rm pl}$	–		–		0.81 ± 0.03	
Fit Quality	C/d.o.f.	292/285		298.16/287		300/284	
		1.03		1.04		1.06	

Note: f denotes parameter is fixed, p denotes parameter error is pegged at upper limit.

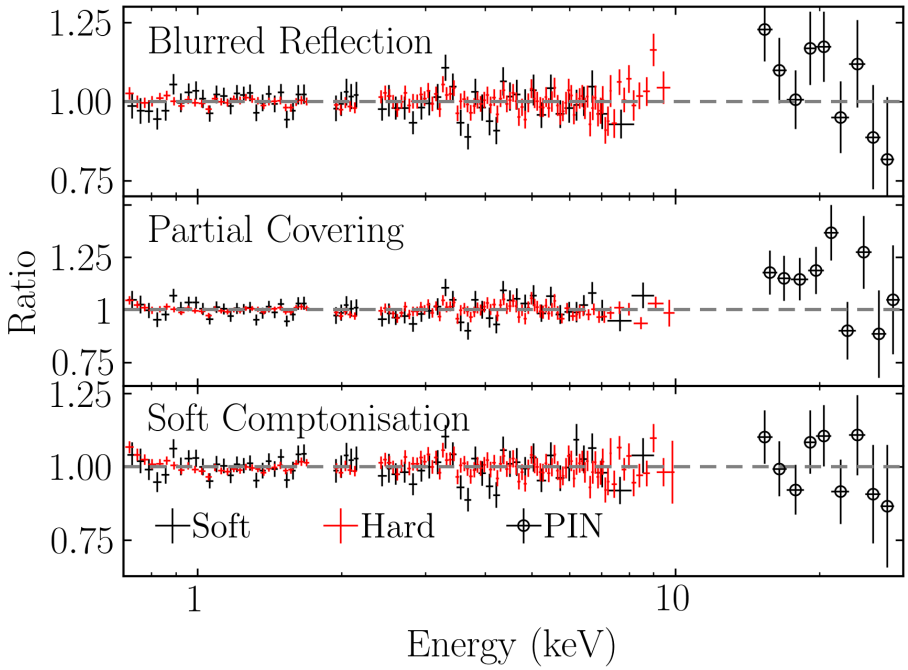

Figure 2.5: Ratio residuals of the soft and hard spectral states fit with the three investigated models.

We tested for other parameter combinations to explain the spectral state change. For example, varying the photon index and ionisation parameter found that the change could be accounted for, though the fit is worse than the presented one. It was found, however, that by allowing ionisation parameter and reflection fraction free to vary between the spectra and linking the photon index in the soft and hard state, the spectral change could not be easily accounted for. That is to say that changes solely in the reflection component cannot cause the observed state change and therefore the photon index of the power law must change during the transition from the soft state to hard state.

2.6.2 Partial covering

The soft and hard spectra were then fit with the partial covering model (Section 2.5.2), again keeping all parameters frozen to the value obtained from fitting the average spectrum with the exception of those listed in Table 2.2 (where frozen parameters are also indicated with a superscript f). Here we find that by allowing covering fraction of the ionised absorber to vary between the two states we can model the spectral state change quite well (C/d.o.f. = 298/287) as shown by the ratio residuals in the middle panel of Figure 2.5. By increasing the covering fraction between the soft and hard states the lower energy ranges of the spectrum become more absorbed, thus hardening the spectrum and producing the state change.

Here we tested a wide variety of parameter combinations in order to explain the spectral variability. At no point was the column density of either absorber found to change significantly between states, hence the freezing of these values in the final fit. The same was found to be true for the ionisation parameters of both absorbers as well as the covering fraction

of the neutral absorber. Allowing the photon index of the power-law to vary between states was not found to improve the fit significantly. Thus, the simplest explanation of the spectral state change using a partial covering model describes a scenario in which the ionised absorber obscures more of the primary X-ray emission therefore hardening the spectrum.

2.6.3 Soft Comptonisation

Finally, the soft Comptonisation model was fit to the soft and hard spectra, the results of which are shown in Table 2.2. The best fit was obtained by letting photon index and Eddington ratio vary freely between the soft and hard states. Freeing only one of those parameters (e.g. Mallick et al. 2017) resulted in poor fits. Electron temperature, optical depth, $f_{\rm pl}$, as well as normalisation of the torus were free parameters which were linked between the two states. All other parameter values were kept frozen to the values obtained from the fitting the average. Ratio residuals of this fit are shown in the bottom panel of Figure 2.5.

We see that changes in the Eddington ratio and power-law index are able to model the spectral changes reasonably well with a statistic of $C/\text{d.o.f.} = 300/284$, and no significant residuals remain.

2.7 Phase-Resolved Variability

In addition to the transition from a soft to hard state evident in the hardness ratio, there is more subtle spectral variability tied to the apparent sinusoidal variations (see Figure 2.1). Considering the hard state alone to isolate this mode of variability and to avoid contamination from the soft/hard variability, we considered only spectra C, D, and E for this portion of the analysis. In an attempt to uncover the underlying mechanism driving the oscillatory behaviour, we took the difference of spectra C, D, and E as shown in Figure 2.6. This revealed that these phase-resolved spectra differ only at lower energies, indicating that the oscillatory behaviour in the $1-3$ keV band discovered in Figure 2.1 is the primary driver of variability during these times. Any changes found between these three spectra is thus associated with the oscillatory behaviour.

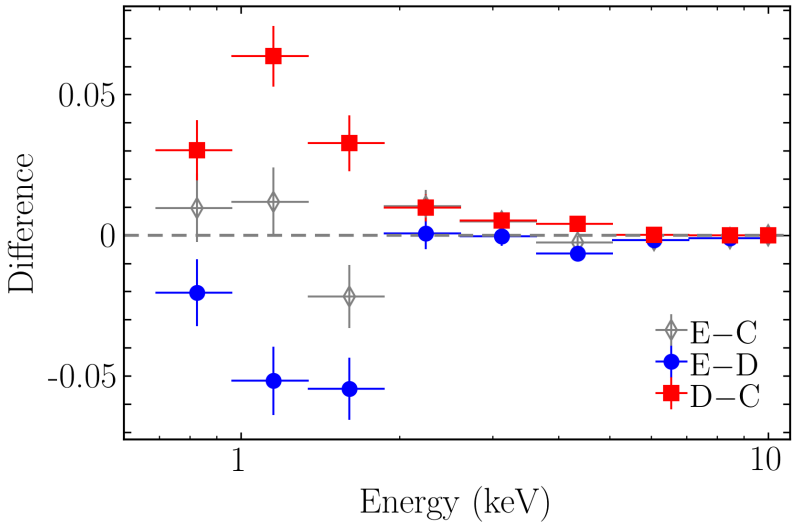

Figure 2.6: Difference between phase-resolved spectra C, D, and E. Significant differences between segments E and D as well as D and C are present at low energies, while there is little difference between segments E and C.

In an attempt to uncover the driver behind this variability, we modelled the C, D, and E phase-resolved spectra, leaving out A and B as they exist in soft and transitional spectral states, respectively. We fit the spectra with the blurred reflection and partial covering models for a variety of parameter combinations. We omitted the soft Comptonisation model from this portion of the analysis as we found it difficult to justify changes in this model over such short timescales, as variations in the physical parameters of the corona (e.g. accretion rate, electron temperature, optical depth) would be expected to change more slowly than $\sim$40 ks.

Both models could replicate the changes in the spectra, but the difference between measured parameters in spectra C, D, and E are insignificant. No strong statement can be made as to the origin of the variability in the $1 - 3$ keV band.

2.8 Discussion

2.8.1 The Fe Kα region

The Fe Kα region could be well-fitted with a single narrow Gaussian at 6.4 keV and a broader Gaussian profile ($\sigma = 400 \pm 200$ eV) at 6.7 keV. Broad, ionized lines, presumably originating from the accretion disc have been proposed in some objects (e.g. Pounds et al. 2001; Reeves et al. 2001). The corresponding full-width at half-maximum of this broad line corresponds to a velocity of approximately 40000 km s^{-1}, which is much greater than the velocities seen in the Balmer lines of Mrk 530 ($\sim$ 6000 km s^{-1}, Kollatschny et al. 2000). Such a velocity would place the origin of this line between the BH and the broadline region, likely in the accretion disc.

Alternatively, the Fe Kα region can be well-fitted with a complex of narrow features, independent of the continuum model used to fit the broadband spectrum. A 6.4 keV Fe I Kα line and narrow ionised Fe XXV Kα and Fe XXVI Kα lines at 6.7 keV and 6.97 keV, respectively, are able to account for all excess residuals in the Fe Kα region with good fit quality (Section 2.4.3). In this scenario, the origin of these emission lines is beyond the inner accretion disc, as all lines are narrow and have not been relativistically broadened by the effects of the SMBH. These narrow lines thus arise from Compton-thin material (such as the Broad or Narrow Line Region), or Compton-thick material (such as the torus) (Matt et al. 2001).

The data are consistent with a Compton shoulder at 6.3 keV which points to an origin from Compton-thick matter like the torus (Matt et al. 1991, 1996b). The lines could originate

from fluorescence and resonant scattering in a highly ionised outer layer of photoionised matter in the torus (Matt et al. 1996a; Bianchi & Matt 2002; Costantini et al. 2010). The equivalent width of the lines in Mrk 530 are consistent with originating from photoionised material (Bianchi & Matt 2002). Though the data do not require inclusion of the Compton shoulder, the torus as the origin of the narrow lines is physically realistic as Mrk 530 is classified as a Seyfert 1.5, so we are observing the system at high inclination and seeing much of the torus. The scenario is consistent with observations of other sources like NGC 5506, an intermediate Seyfert with a complex Fe region (Bianchi & Matt 2002), and Mrk 279, a Seyfert 1 with ionised lines likely originating from the tours (Costantini et al. 2010). A future mission like XARM, with Hitomi-like (Takahashi et al. 2016) spectral resolution will advance this work.

2.8.2 The broadband X-ray spectrum and variability

The X-ray spectrum of Mrk 530 transitions smoothly from a power law to a soft excess at about $E < 2$ keV. The iron line complex exhibits no strong evidence of a relativistically broadened Fe Kα emission line and any hard excess emission above 10 keV that could be associated with a Compton hump is also weak. As such, the source spectrum is reminiscent of complicated sources like Akn 120 (e.g. Matt et al. 2014).

The X-ray continuum of Mrk 530 could be well-fitted with a number of physical models like blurred reflection, partial covering, and soft Comptonisation. None of the models could be distinguished by quality of fit.

In the partial covering and Comptonisation scenarios, the bulk of the emission above

10 keV is fitted with the PEXMON component that is used to mimic distant reflection from the cold torus. In the blurred reflection scenario, the PEXMON component is weaker as the blurred reflector contributes to some of the high-energy emission.

However, the reflection fraction in the blurred reflector model is below unity ($R \approx 0.22$), which is consistent with anisotropic emission away from the accretion disc (e.g. Gonzalez et al. 2018). This could be beamed emission that arises in the base of a jet (e.g. Gallo et al. 2015; Wilkins & Gallo 2015b), but radio studies of Mrk 530 (e.g. Lal et al. 2011) have not revealed evidence of a jet component. The need for a shallow emissivity profile in the X-ray model also indicates that any point-like corona would be located at relatively large distances from the black hole and not strongly influenced by light bending effects.

During the course of this *Suzaku* observation, Mrk 530 exhibited two distinct spectral states: a soft state which smoothly transitioned to a hard state. The variability between these two states can be well-described by a blurred reflection model with changes in photon index and reflection fraction between the two states (Section 2.6.1). The photon index is greater (steeper) for the soft state, and lower (flatter) for the hard state. The change in photon index indicates changes in the corona (e.g. temperature, density), or could be attributed to changes in velocity if the source is indeed moving away from the disc (e.g. Gonzalez et al. 2018), which would also result in changes in the reflection fraction.

The spectral state change can also be explained through a partial covering scenario with changes in covering fraction of an ionised absorber (Section 2.6.2). Here the hard state sees an increase in the covering fraction which attenuates low-energy emission, effectively hardening the spectrum. The covering fraction itself can represent a single patchy cloud or

numerous individual clouds. Therefore, a change in covering fraction could also indicate a change in the number of clouds along the line of sight.

Alternatively, the spectral state change could be explained with a soft Comptonisation model that changes in photon index and Eddington ratio (Section 2.6.3). As was the case for the blurred reflection model, the photon index was found to be greater for the soft state and lower for the hard state, indicating changes in the primary emitter between the states.

This model produced a lower Eddington ratio along with a steeper power-law during the soft state, exhibiting the softer-when-brighter behaviour frequently observed in Seyfert galaxies (e.g. Shemmer et al. 2006; Sobolewska & Papadakis 2009). However, understanding the rapid changes in the Eddington ratio is difficult.

It is plausible that the spectral variability in Mrk 530 is not due to simply one of these examined models, but rather some combination of them (e.g. Parker et al. 2018).

2.8.3 Light curve variability

The light curve displays variations that resemble two cycles of a sinusoidal function. Though a sinusoid fit to the data is not statistically significant ($\chi^2_\nu = 2.57$), the oscillations have a period of $T \approx 86$ ks, which for a BH mass of 1.15×10^8 $M_\odot$ (Woo et al. 2012), is consistent with the dynamical timescale at $\sim 10\ r_g$ in a standard accretion disc. The radius is completely consistent with where we expect X-ray emission to be coming from. However, it has been shown that ordinary red noise can commonly mimic a few cycles of sinusoidal behaviour (Vaughan et al. 2016). In cases of robust detection of periodicity, the QPO behaviour has been detected in a narrow band in addition to broadband aperiodic

variability. For example, the QPO behaviour in RE J1034+396 does not dominate the red noise variability, but appears in addition to it (Gierliński et al. 2008).

Halpern & Marshall (1996) observed the Seyfert 1 galaxy RX J0437.4 − 4711 with the *EUVE* satellite and found the object to exhibit periodic behaviour in the soft X-ray regime ($0.12-0.18$ keV) with a period of ~ 0.9 days, which they note could correspond to an orbital timescale around such a SMBH. Halpern et al. (2003) found this detection to be significant on the > 95 per cent level.

To ensure that the field around Mrk 530 was free of contamination from variable sources, the surrounding field of view was checked for other objects that could be contributing to this periodic detection. Two X-ray sources that lay within the source extraction radius were found, 2XMM J231856.1 + 001403 and 2XMM J231857.3 + 001341. However, the flux of these sources was found to be negligible (5.5×10^{-13} erg cm^{-2} s^{-1} and 1.1×10^{-13} erg cm^{-2} s^{-1} in the $0.2-12$ keV band) compared to the flux of Mrk 530 (4.3×10^{-11} erg cm^{-2} s^{-1} in the same band), and so these sources can be confidently discounted as the source of variability in this observation.

2.9 Conclusions

Mrk 530 was observed by *Suzaku* and found to exhibit two distinct types of variability during the course of the observation: a spectral state change which transitioned smoothly from a soft state to a hard state, and apparent sinusoidal variability in a narrow energy band.

To characterise the average spectrum of the observation as well as the spectral changes between the soft and hard states, three different physical models were fit to the data: a blurred reflection model, a partial covering model, and a soft Comptonisation model. All three models were able to describe the average spectrum and changes between the two spectral states reasonably well. Fits to the Fe Kα band favour multiple narrow emission lines likely originating from neutral and ionised material in the distant torus.

The apparent periodicity in the light curve is statistically insignificant. We were interested in the driver behind this variability given that the period corresponds to the orbital timescale of the BH at a radius of $\sim 10\ r_g$. However, we were unable to constrain the driver of this variability with current data quality.

Deeper observations over a broader band will provide the opportunity to distinguish various continuum models and further investigate continuum flux variability.

Chapter 3

A Timing Analysis of Markarian 335

3.1 Introduction

Active Galactic Nuclei (AGN) are galaxies that contain a supermassive black hole ($\sim 10^6 - 10^9$ $M_\odot$) at their centre that is actively emitting electromagnetic radiation through an accretion process. AGN are some of the most luminous astrophysical sources, with bolometric luminosities up to $\sim 10^{13}$ $L_\odot$ and higher. The emission from the central regions of AGN is extremely variable. Their brightness can change by orders of magnitude on short timescales (e.g. minutes to hours) to long timescales (e.g. decades) and everything in between. Short timescale variability is seen in the X-ray band, where X-ray emission, coming from the central-most region of the AGN varies over minutes and hours, and can change in flux by an order of magnitude over the course of a single observation (typically $\sim$ 100 ks).

For such a massive object to exhibit such rapid variations is remarkable; understanding the nature of this variability can provide insight on the physics of some of the most energetic objects in the Universe. Studying X-ray emission from the inner regions of AGN can help us to understand the behaviour of these remarkable objects and learn about the physics and processes that govern them.

One such way we can study AGN is through timing analyses (more in Section 3.2), which utilise information contained in the light curves (changes in flux or photon counts over time). By analyses of X-ray light curves we can gain insight into the processes and geometry of the central region of AGN.

Markarian 335 (hereafter Mrk 335) is a well-studied Narrow-Line Seyfert 1 galaxy at a redshift of $z = 0.026$. It contains a supermassive black hole with a mass of 2.6×10^7 $M_\odot$ (Grier et al. 2012). Mrk 335 is an extremely bright AGN and so has been observed by multiple X-Ray telescopes (e.g. *XMM-Newton*, *Suzaku*, *Swift*, *NuSTAR*) and featured in many studies, as far back as the 1970's (e.g. Dibai 1979). Prior to 2007, Mrk 335 was a bright AGN that exhibited typical levels of X-ray emission compared to its UV luminosity (e.g. Gondoin et al. 2002; Longinotti et al. 2007). A 2007 observation taken by the *Swift* and *XMM-Newton* satellites revealed that Mrk 335 had dropped in X-ray flux by an order of magnitude and entered an X-ray low flux-state (Grupe et al. 2007). Even when in a low flux state, Mrk 335 is relatively bright and telescopes are able to collect adequate photon counts due to its proximity (Wilkins & Gallo 2015a). Though it has entered into a low-flux state, Mrk 335 frequently exhibits short-lived outbursts or flares where it brightens by factors of > 10 and then drops down again (e.g. Grupe et al. 2012; Gallo et al. 2013, 2019).

Previous work on Mrk 335 has found that the X-ray spectra are described and dominated by relativistically blurred reflection (Gallo et al. 2013; see also Section 1.3.2). Some studies have also found evidence for absorption features caused by outflowing material (Longinotti et al. 2013), while others have found no such evidence (Larsson et al. 2008).

During the 2009 intermediate flux state of Mrk 335, it was observed in two consecutive orbits by the *XMM-Newton* X-ray satellite. Analysis by Gallo et al. (2013) found through spectral modelling a change in the mode of variability during the first of these observations. For the first 70 ks of the observation, the spectral variability was found to be well-described by changes in flux of the primary emitter, while after 70 ks, changes in the spectral slope of the primary emitter and the reflected flux also contribute to the variability. The work of Ehler (2017) corroborated these findings by identifying a change in the mode of variability at $\sim$ 70ks using flux-flux plots, a model-independent technique that probes variability.

Mrk 335 has exhibited extreme variability on all timescales. This work examines the nature of the short-term variability by implementing timing methods. We seek to understand the nature of the large flux drop from pre- and post-2007, and the rapid variability in 2009. In Section 3.2, we introduce and describe the timing methods used in this analysis. In Section 3.3 we list the observations of Mrk 335 that we analysed along with our processing techniques. Section 3.4 presents our current timing analysis of Mrk 335, which is a still a work in progress. As such, Section 3.5 discusses future steps to be taken with this work.

3.2 Timing Processes

3.2.1 Stationarity

Variability in AGN, particularly Seyfert 1 AGN, can occur as a result of two different types of processes: stationary and non-stationary. A stationary process is one for which statistical parameters of a time series (or light curve) such as the mean and variance do not change in time. A stationary process is a stochastic or random process such as noise. AGN tend to be red noise ($P \propto f^{-2}$) dominated and are expected to exhibit stationary behaviour.

For a stationary light curve (Figure 3.1, left panel), the mean of $x(t)$ for a given segment of the light curve (e.g. $t_0 \rightarrow t_1$) is the same as the mean of the whole time series ($x_{\rm mean}$); the light curve varies around the mean, returning to the mean value often. In the context of AGN, stationarity, or noise, is intrinsic to the source and is a consequence of the accretion process. An AGN with a light curve having stationary properties means that it was produced by stochastic means; the variability present in the light curve is simply a result of noise in the accretion process.

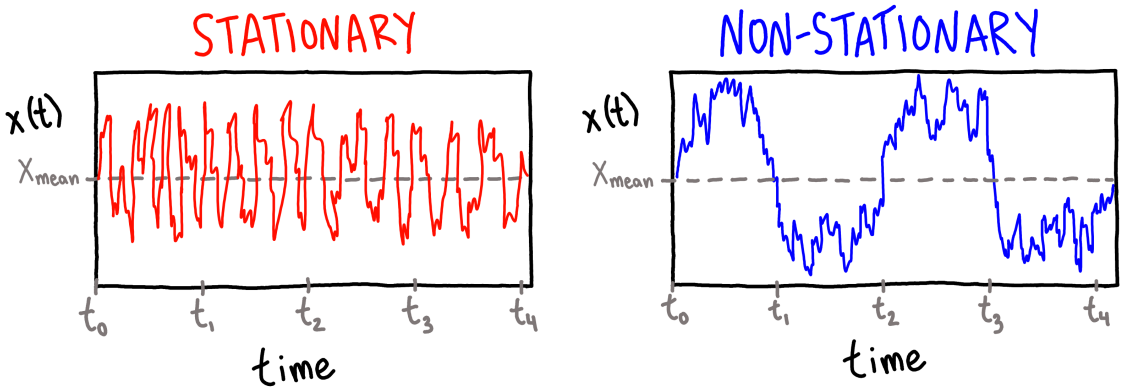

Figure 3.1: Examples of stationary (*left panel*) and non-stationary (*right panel*) time series.

On the other hand, a non-stationary process is a process for which the statistical properties are not constant in time. For a time series (or light curve) of a non-stationary process (Figure 3.1, right panel), the mean of $x(t)$ for a given segment is *not* the mean of the whole series. For example, you can see from the figure that the mean of $x(t)$ from $t_0 \rightarrow t_1$ is not the same as x_{mean}. An AGN with a light curve having non-stationary properties indicates that the variability was produced by changes in the underlying processes, rather than just noisy fluctuations, i.e. there is some physical change in the system that is driving the variability (Vaughan et al. 2003). Determining whether the variability in a source is produced by stationary or non-stationary processes allows us to discern the physical mechanisms at work and better understand the accretion process and changes in the central region.

Vaughan et al. (2003) present a method of determining stationarity of AGN light curves by looking at statistical properties of the light curve. They showed that the light curve of stationary process can still have a variance or mean that changes over time; fluctuations in variance are not sufficient to claim the variability process is non-stationary. A light curve is a single realisation of the process producing it, so while the process may be stationary, a single realisation of it may not be. We thus must consider the *expectation value* of the statistical properties to probe the stationarity. The expectation value should provide insight on the underlying process rather than a single realisation of that process (Bendat & Piersol 1986).

From Vaughan et al. (2003), the variance (S^2) of a light curve is:

$$S^2 = \frac{1}{N-1}\sum_{i=1}^{N}(x_i - \bar{x})^2 \tag{3.1}$$

where $\bar{x}$ is the arithemetic mean of the flux x_i, and each segment should contain at least 20 points ($N \gtrsim 20$) to obtain meaningful results. This equation, however, assumes no measurement error, while in reality there is measurement error associated with obtaining the light curve (e.g. Poisson noise). As such, we must subtract from the variance the measurement error ($\overline{\sigma^2_{\rm err}}$) to obtain the excess variance ($\sigma^2_{\rm XS}$):

$$\sigma^2_{\rm XS} = S^2 - \overline{\sigma^2_{\rm err}} \tag{3.2}$$

where:

$$\overline{\sigma^2_{\rm err}} = \frac{1}{N}\sum_{i=1}^{N}\sigma^2_{{\rm err},i} \tag{3.3}$$

The excess variance (Nandra et al. 2007; Edelson et al. 2002), having removed the measurement uncertainty, thus measures the variance intrinsic to the source.

$F_{\rm var}$ is the fractional root-mean-square (rms) variability amplitude (Edelson et al. 1990; Rodríguez-Pascual et al. 1997). It normalises the excess variance by the count rate and gives the fractional variability as a percentage:

$$F_{\rm var} = \sqrt{\frac{\sigma^2_{\rm XS}}{\bar{x}^2}} \tag{3.4}$$

To examine the stationarity of a light curve, we must then take the expectation value of these parameters ($\sigma^2_{\rm XS}$, $F_{\rm var}$) over the observation. Vaughan et al. (2003) note that you can average M excess variance points to produce an average excess variance ($\langle\sigma^2_{\rm XS}\rangle$) with the uncertainty obtained by standard error: $\sigma_\mu = \sigma/\sqrt{M}$ (Bevington 1992). For robust results, each average should contain at least 20 points ($M \gtrsim 20$). Recalling that each variance estimate also required $N \gtrsim 20$, this method of determining stationarity requires a large amount of data with at least 400 data points necessary to yield a single estimate of the mean variance (Vaughan et al. 2003). In X-ray observations of AGN, such large data sets can be hard to come by, as photon counts are quite sparse and we must heavily bin-up our light curves.

Another method of determining the stationarity of a light curve is by looking at the distribution of the count rate. A lognormally distributed count rate is expected of a stationary process, as the distributions of accreting systems typically exhibit lognormal behaviour (e.g. Uttley et al. 2005; Edelson et al. 2013; Alston et al. 2019). Table 3.1 summarises the different properties of stationary and non-stationary processes.

Table 3.1: Characteristics of stationary and non-stationary processes.

Stationary	**Non-Stationary**
expectation values of statistical parameters are constant	expectation values of statistical parameters are not constant
count rate distribution is lognormal	count rate distribution is not lognormal
PSD does not change over time	PSD changes over time

3.2.2 Power Density Spectrum

The power density spectrum (PSD; PDS) measures the power of the variability as a function of Fourier frequency. Through it we are able to see how different energy bands behave on different timescales.

A PSD utilises a Fourier transform to determine the frequencies which are contributing most to the power. Any time series can be broken into a sum of sine waves (Figure 3.2, left panel), just as the black function in the figure is the sum of the blue, red, and green sine curves. Each of those sine waves has a frequency, and a power spectrum (Figure 3.2, right panel) shows which frequencies are the most dominant in the time series.

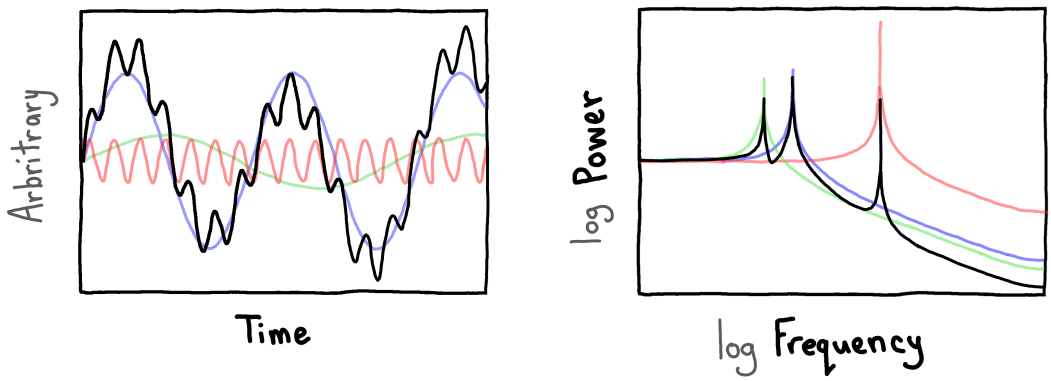

Figure 3.2: *Left panel:* Time series showing a simple function (black) and the sine waves that comprise it (blue, red, green). *Right panel:* Power spectrum of the left panel, showing the frequencies from the three constituent sine waves that contribute to the time series.

The PSDs of most AGN are described well by a broken power-law model with slope ~ -1 at lower frequencies (below the break) and slope ≤ -2 at higher frequencies (above the break) (Arévalo et al. 2008a). The break frequency at which this transition occurs can

reveal information about the black hole such as black hole mass, and possibly accretion rate or obscuration along the line-of-sight (Uttley & McHardy 2005; McHardy et al. 2006; González-Martín & Vaughan 2012; González-Martín 2018). Vaughan et al. (2003) note that if the variability observed in an AGN is the result of a stationary process, then the PSD will not change over time, while a changing PSD indicates that there are changes in the underlying process producing the variability (i.e. a non-stationary process). Comparing PSDs across different observations can thus provide insight as to whether the variability in a specific AGN is the result of a stationary or non-stationary process.

Uttley et al. (2014) presented a recipe for computing the power density spectrum for an X-ray light curve. Assuming the light curve is background-subtracted, the first step is to take the discrete Fourier transform (DFT) of the light curve:

$$X_n = \sum_{k=0}^{N-1} x_k \exp 2\pi nk/N \tag{3.5}$$

where x_k is the kth value of the light curve, N is the number of time bins (they must be contiguous), and X_n is the discrete Fourier transform at each frequency. The Fourier frequencies are given by $f_n = n/(N\Delta t)$ where $n = 1, 2, 3, \ldots N/2$. The minimum frequency is thus the inverse of the observation length: $f_{\rm min} = 1/N\Delta t = 1/T_{\rm obs}$ while the maximum frequency is the Nyquist frequency: $f_{\rm max} = 1/(2\Delta t)$. The upper limit of n is $N/2$ and not N, because in order to detect any changes we must measure something twice. Since Δt is the time resolution, $2\Delta t$ is thus the shortest detectable timescale for variability (Kolb 2010).

The next step in making a PSD is to construct the periodogram via:

$$|X_n|^2 = X_n^* X_n \tag{3.6}$$

where $*$ denotes complex conjugation. Finally, the periodogram is normalised:

$$P_n = \frac{2\Delta t}{\langle x \rangle^2 N} |X_n|^2 \tag{3.7}$$

where $\langle x \rangle$ is the or count rate of the light curve and P_n is the normalised periodogram. This produces the raw PSD, which is customarily then binned-up. The Poisson noise level ($P_{\rm noise}$) of the PSD can be calculated via:

$$P_{\rm noise} = \frac{2(\langle x \rangle + \langle b \rangle)}{\langle x \rangle^2} \tag{3.8}$$

where $\langle b \rangle$ is the average count rate of the background light curve.

3.2.3 RMS Spectrum

The rms spectrum was pioneered by Revnivtsev et al. (1999). It measures the rms (root-mean-squared) variability amplitude in a light curve as a function of energy, and is frequency-resolved, so allows one to probe specific timescales. By calculating the rms variability in adjacent energy bands and constructing a spectrum, one can model the variability spectrum and determine the component(s) contributing to the variability.

Arévalo et al. (2008a) describe how to construct a frequency-dependent RMS spectrum. The first step is to obtain the normalised excess variance ($\sigma^2_{\mathrm{NXS},\Delta f}$) by integrating the PSD over a desired frequency range (Δf) after P_{noise} has been subtracted from the PSD. However, since realistic power spectra are discrete we can perform a discrete sum over the integers a and b:

$$\sigma^2_{\mathrm{NXS},\Delta f} = \sum_{i=a}^{b} (P(f_i) - P_{\mathrm{noise}})\delta f \tag{3.9}$$

where δf is the inverse of the light curve length ($\delta f = 1/T_{\mathrm{obs}}$). The error on the normalised excess variance can be calculated via:

$$\mathrm{err}(\sigma^2_{\mathrm{NXS},\Delta f}) = \sqrt{\left(\frac{P_{\mathrm{noise}} \times \Delta f}{\sqrt{N'}}\right)^2 + \frac{2P_{\mathrm{noise}} \times \Delta f \sigma^2_{\mathrm{NXS},\Delta f}}{N'}} \tag{3.10}$$

where N' is the number of periodogram points in Δf. Constructing light curves in many adjacent energy bands and calculating $\sigma^2_{\mathrm{NXS},\Delta f}$ allows one to construct a normalised excess variance spectrum for the desired frequency range. The Δf subscripts denoting the frequency-dependence are often dropped for simplicity. Arévalo et al. (2008a) note that a flat σ^2_{NXS} spectrum signifies that the variability amplitude in each energy band is proportional to its flux, while a dip in the σ^2_{NXS} spectrum denotes a constant component present in that energy range.

The rms variability, which is not normalised by count rate, can be then computed from the normalised excess variance via:

$$\sigma_{\mathrm{rms},\Delta \mathrm{f}} = \bar{x}\sqrt{\sigma^2_{\mathrm{NXS},\Delta f}} \tag{3.11}$$

for each energy band, where $\bar{x}$ is the average count rate in the given energy band. The error on the rms can be calculated via:

$$\mathrm{err}(\sigma_{\mathrm{rms},\Delta f}) = \sqrt{\sigma^2_{\mathrm{NXS},\Delta f} + \mathrm{err}(\sigma^2_{\mathrm{NXS},\Delta f})} - \sigma_{\mathrm{rms},\Delta f} \tag{3.12}$$

Calculating this for adjacent energy bands allows one to construct an rms spectrum. Arévalo et al. (2008a) note that because the rms spectrum is normalised, it is unaffected by any constant spectral components (unlike the σ^2_{NXS} spectrum).

3.2.4 Covariance Spectrum

The covariance spectrum, pioneered by Wilkinson & Uttley (2009), is similar to the rms spectrum, but rather than measuring the total intrinsic variability, measures only the variability that is correlated with some reference energy band. It utilises the cross-spectrum of different energy bands with the reference band to show the spectral shape of the variable components correlated with the reference band (Uttley et al. 2014). The covariance spectrum has higher signal-to-noise than the rms spectrum. It is frequency-resolved and thus can show what components in a given frequency range are varying with the reference band.

Uttley et al. (2014) present a detailed recipe for constructing a covariance spectrum, which we will summarise here:

1. Make light curves (source, x, and background) for the reference energy band (e.g. broadband).

2. Make light curves (source and background) for each energy band that the spectrum

will be composed of; we will call these "CI" light curves (for channel of interest). Make sure the time sampling (length and binning) of these light curves are all the same, and also the same as the reference light curve.

3. If the reference band contains the energy band of the CI light curve, subtract the CI light curve from the reference light curve to create a corrected reference light curve (y). Do this for each CI light curve that is contained within the reference band, and do this for the background light curves as well.

4. For each CI, obtain the PSD of the CI light curve as well as the corrected reference light curve. (See section 3.2.2 for how to construct a PSD.) Do not subtract $P_{\rm noise}$ or bin up the PSD.

5. Obtain the cross-spectrum for each CI via:

$$C_{XY,n} = X_n^* Y_n \tag{3.13}$$

where X_n is the DFT of the CI light curve, Y_n is the DFT of the corrected reference light curve and $*$ denotes complex conjugation.

6. Average the PSDs ($\bar{P}_X$, $\bar{P}_Y$) and cross-spectrum ($\bar{C}_{XY}$) over a selected broad frequency range $\Delta\nu_j$ (e.g. below or above break frequency) for each CI.

7. Calculate the covariance for each CI via:

$$C_\nu(\nu_j) = \langle x \rangle \sqrt{\frac{\Delta\nu_j(|\bar{C}_{XY}(\nu_j)|^2 - n^2)}{\bar{P}_Y(\nu_j) - P_{Y,\rm noise}}} \tag{3.14}$$

which includes n^2, a bias term due to Poisson noise contamination:

$$n^2 = [(\bar{P}_X(\nu_j) - P_{X,\text{noise}})P_{Y,\text{noise}} + (\bar{P}_Y(\nu_j) - P_{Y,\text{noise}})P_{X,\text{noise}} + P_{X,\text{noise}}P_{Y,\text{noise}}]/KM \tag{3.15}$$

Additionally, $\langle x \rangle$ is the average count rate of the CI light curve, $\Delta\nu_j$ is the frequency width of the bin that was averaged over, K is number of frequencies (or data points) per segment, and M is the number of segments that were averaged over.

8. Calculate the covariance error for each CI via:

$$\Delta C_\nu(\nu_j) = \sqrt{\frac{[C_\nu(\nu_j)]^2\sigma^2_{Y,\text{noise}} + \sigma^2_Y(\nu_j)^2\sigma^2_{X,\text{noise}} + \sigma^2_{X,\text{noise}}\sigma^2_{Y,\text{noise}}}{2KM\sigma^2_Y(\nu_j)}} \tag{3.16}$$

which utlises the rms spectrum of the corrected reference band ($\sigma^2_Y(\nu_j)$), where:

$$\sigma^2_Y(\nu_j) = (P_Y(\nu_j) - P_{Y,\text{noise}})\langle x \rangle^2 \Delta\nu_j$$

$$\sigma^2_{Y,\text{noise}} = P_{Y,\text{noise}}\langle y \rangle^2 \Delta\nu_j$$

$$\sigma^2_{X,\text{noise}} = P_{X,\text{noise}}\langle x \rangle^2 \Delta\nu_j$$

9. Plot the covariance (and error) over each CI energy band to construct the covariance spectrum.

3.2.5 Lag-frequency Spectrum

A lag-frequency spectrum measures the time lag between different energy bands in different frequency ranges (e.g. Zoghbi et al. 2010; Jin et al. 2017). Time lags can arise due to light travel time in regions around the black hole (reverberation lags), or can be a result of changes in the corona. They can provide insight into the physical distances and geometries of the inner black hole region. (e.g. Uttley et al. 2014; Wilkins et al. 2016). The magnitude of the lag scales linearly with black hole mass (e.g. Wilkins et al. 2016). This suggests that the size scale of the process producing the lag is the same across AGN.

Uttley et al. (2014) present a recipe for constructing a lag-frequency spectrum, which is very similar to the procedure for constructing a covariance spectrum. For the lag-frequency spectrum, light curves in only two energy bands are used: $x(t)$ and $y(t)$. The bands are chosen based on what you are trying to probe (more below). The cross-spectrum is then calculated (see Equation 3.13), and binned up over Fourier frequencies (ν_j) and averaged over light curve segments in order to reduce the effects of noise, using the following equation:

$$\bar{C}_{XY}(\nu_j) = \frac{1}{KM} \sum_{n=i}^{i+K-1} \sum_{m=1}^{M} C_{XY,n,m} \tag{3.17}$$

From the binned cross spectrum, we can determine the average phase-shift $\bar{\phi}_n$ between the two bands:

$$\bar{C}_{XY,n} = \bar{A}_{X,n}\bar{A}_{Y,n} \exp(i\bar{\phi}_n) \tag{3.18}$$

where $A_{X,n}$ and $A_{Y,n}$ are the amplitudes of the Fourier transform of light curves $x(t)$ and $y(t)$, respectively. Finally, the phase-shift is utilised in the following equation to obtain the time lag $\tau(\nu_j)$:

$$\tau(\bar{\nu}_j) = \bar{\phi}(\nu_j)/(2\pi\nu_j) \tag{3.19}$$

where $\bar{\phi}(\nu_j)$ is the average phase lag between the two light curves in the ν_j frequency bin, where ν_j is the midpoint frequency in that bin. The error on the time lag ($\Delta\tau$) is given by:

$$\Delta\tau = \Delta\phi/(2\pi\nu_j) \tag{3.20}$$

where $\Delta\phi$ is the error on the phase lag:

$$\Delta\phi(\nu_j) = \sqrt{\frac{1-\gamma^2(\nu_j)}{2\gamma^2(\nu_j)KM}} \tag{3.21}$$

which implements the coherence γ^2 in the frequency bin ν_j. The coherence (Vaughan & Nowak 1997) is the degree to which the light curves are simply a linear transformation of one another; two identical light curves that are shifted in time will have a coherence of 1. The coherence is reduced as uncorrelated variability (such as Poisson noise) is introduced to the two light curves independently. The coherence is defined by:

$$\gamma^2(\nu_j) = \frac{|\bar{C}_{XY}(\nu_j)|^2 - n^2}{\bar{P}_X(\nu_j)\bar{P}_Y(\nu_j)} \tag{3.22}$$

where n^2 is the bias term defined in Equation 3.15, and $\bar{P}_X(\nu_j)$ and $\bar{P}_Y(\nu_j)$ are the PSDs of the light curves $x(t)$ and $y(t)$, respectively. The PSDs are not Poisson noise subtracted, and should be binned up in the same manner as the coherence (Equation 3.17).

In our case, the bands $x = 1 - 4$ keV and $y = 0.3 - 1$ keV were used so that we could probe the delay of variations in the bands compositing the primary continuum (see Section 1.3.2) and the soft excess (see Section 1.3.3). In this context, a positive lag means that the soft component is leading the variability in the continuum. This means that changes occur in the soft band before occurring in the continuum. A negative lag means that changes in the continuum precede changes in the soft component. Figure 3.3 shows an example of a lag-frequency spectrum made using the same bands to compare the continuum and soft excess. Positive, long timescale lags are attributed to the accretion mechanism, from the inward propagation of material in the disc (e.g. Wilkins et al. 2016). Negative, more rapid lags are a result of light travel time between the corona and disc, i.e. reverberation (e.g. Gallo 2011).

3.2.6 Principal Component Analysis

Principal component analysis (PCA) is a another tool that characterises variability (e.g. Kendall 1975; Parker et al. 2014, 2015; Gallant et al. 2018). It decomposes a spectrum into a set of orthogonal eigenvectors that describe the variability; these eigenvectors are the principal components (PCs) and represent the spectral components that contribute most to the variability. One of the advantages of this method is that it gives the spectra of individual varying components separately, rather than one spectrum that contains all

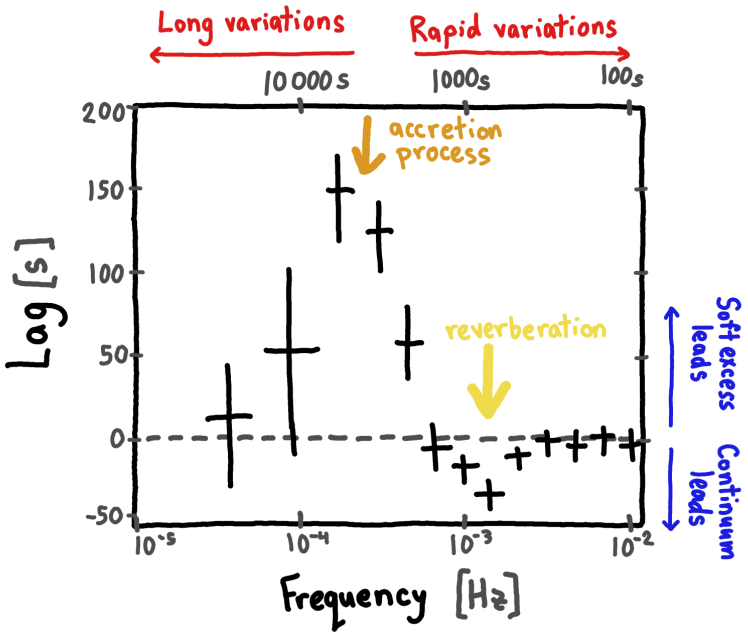

Figure 3.3: Example of a lag-frequency spectrum. Positive lags mean that changes in the soft excess lead changes in the continuum, while negative lags mean that changes in the continuum occur before changes in the soft excess. Positive lags (orange arrow) are attributed to the accretion process, while negative lags (yellow arrow) are a result of reverberation. (Reproduced from Gallo 2011 and Zoghbi et al. 2010.)

varying components (as an rms spectrum would, for example).

To perform a PCA on a given observation, the observation must be broken into equal-length segments and a spectrum made for each segment; this allows the time-dependence of the variability to be probed. The spectral shape of the PCs can be interpreted (e.g. Parker et al. 2015) to determine the spectral component(s) driving the variability.

Figure 3.4 shows an example of principal component spectra. The left panel shows a PC spectrum that is entirely positive. Such a PC spectrum indicates that the variations in all energy bands change together and are correlated. For example, AGN variability could

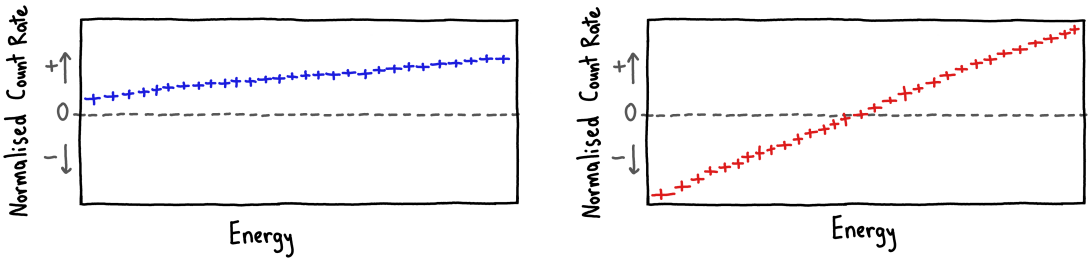

Figure 3.4: Example of principal component spectra. *Left panel:* A PC spectrum indicating that variations in all energy bands change together. *Right panel:* A PC spectrum indicating variability that is anti-correlated at high and low energies.

be caused by changes in the normalisation of the source spectrum. The right panel shows a PC spectrum that crosses 0. This spectrum indicates that variability at high energies is anti-correlated with variability at low energies. For example, changes in the spectral slope of an AGN spectrum would manifest as this. It is important to note that the direction of the y-axis is arbitrary in all PC spectra; whether the spectrum is positive or negative does not matter, only the amplitude of the spectrum and whether it crosses 0. If the spectra of Figure 3.4 were mirrored about the y-axes the interpretations would remain the same.

3.3 Observations & Data Reduction

Mrk 335 has been observed by the X-ray satellite *XMM-Newton* on several occasions, and caught in different flux states. We examine only three of the existing seven observations of Mrk 335 taken by the *XMM-Newton* satellite due to the observation length and data quality necessary to perform these timing studies. Information on these observations is listed in Table 3.2. Reference names note the year and relative flux level of each observation (high and intermediate).

Table 3.2: Observations of Mrk 335 used in this analysis.

Reference Name	Obs ID	Start Date	Exposure	GTI
2006 High	0306870101	2006-01-03	133 ks	132.5 ks
2009 Int 1	0600540601	2009-06-11	132 ks	112 ks
2009 Int 2	0600540501	2009-06-13	82.6 ks	80.7 ks

The data were processed using the *XMM-Newton* Science Analysis System (SAS) v. 15.0.0 to construct event lists. A good time interval (GTI) was constructed for each observation to remove background flaring.

Light curves were constructed for the source from a 35″ circular region centred on the source. Background light curves were generated from a 50″ circular region on the same chip as the source. After checking to ensure their consistency, light curves from the three EPIC detectors (pn, mos1, mos2) were merged using `lcmath` (a HEASARC FTOOL) to obtain a higher signal-to-noise ratio (as was done by Jin et al. 2017). For the 2006 Int 1 observation, the light curve was truncated at 112 ks due to extremely low signal-to-noise beyond that point.

Spectra were created using the same extraction regions as the light curves for both the source and background. The spectra were optimally binned using the method outlined by Kaastra & Bleeker (2016) using the PYTHON code written by C. Ferrigno[1]. Spectral data below 0.3 keV and above 10 keV were omitted due to instrument calibration uncertainty and low sensitivity.

[1] `https://cms.unige.ch/isdc/ferrigno/developed-code/`

3.4 Application of Timing Methods to Mrk 335

3.4.1 Characterising the Variability

Broadband ($0.3 - 10$ keV) EPIC-merged light curves of the three observations binned at 200s intervals are shown in panel 1 of Figures 3.5, 3.6, 3.7, with the dashed line denoting the average count rate of each observation.

To examine the variability of each of these light curves, we followed the method of Vaughan et al. (2003), outlined in Section 3.2.1, to compute the excess variance (panel 2 of Figures 3.5, 3.6, 3.7) and fractional variability (panel 4 of the same figures) for every $N = 20$ points. The light curves were binned by 200s because smaller bin sizes did not produce high enough signal-to-noise to allow us calculate the excess variance and fractional variability (as the error term was larger than the variance).

As noted in Section 3.2.1, the excess variance or fractional variability of a light curve may not reflect its stationarity, so we took the expectation value of these values over the observation. Ideally, one would average every $M = 20$ points to obtain the most robust estimate, however, given that we had to bin our light curves at 200s, if we wanted at least $M = 20$ points per average, we would have only one average value per observation and so could not evaluate the stationarity across the observation. To get around this, we compromised with $M < 20$ to allow for two estimates of $\langle \sigma_{XS}^2 \rangle$ and $\langle F_{\rm var} \rangle$ per observation. For the 2006 High observation we used $M = 16$, while we used $M = 13$ and $M = 10$ for 2009 Int 1 and 2009 Int 2, respectively. The average excess variance is shown in panel 3 of Figures 3.5, 3.6, 3.7, while the averaged fractional variability are shown in panel 5 of the

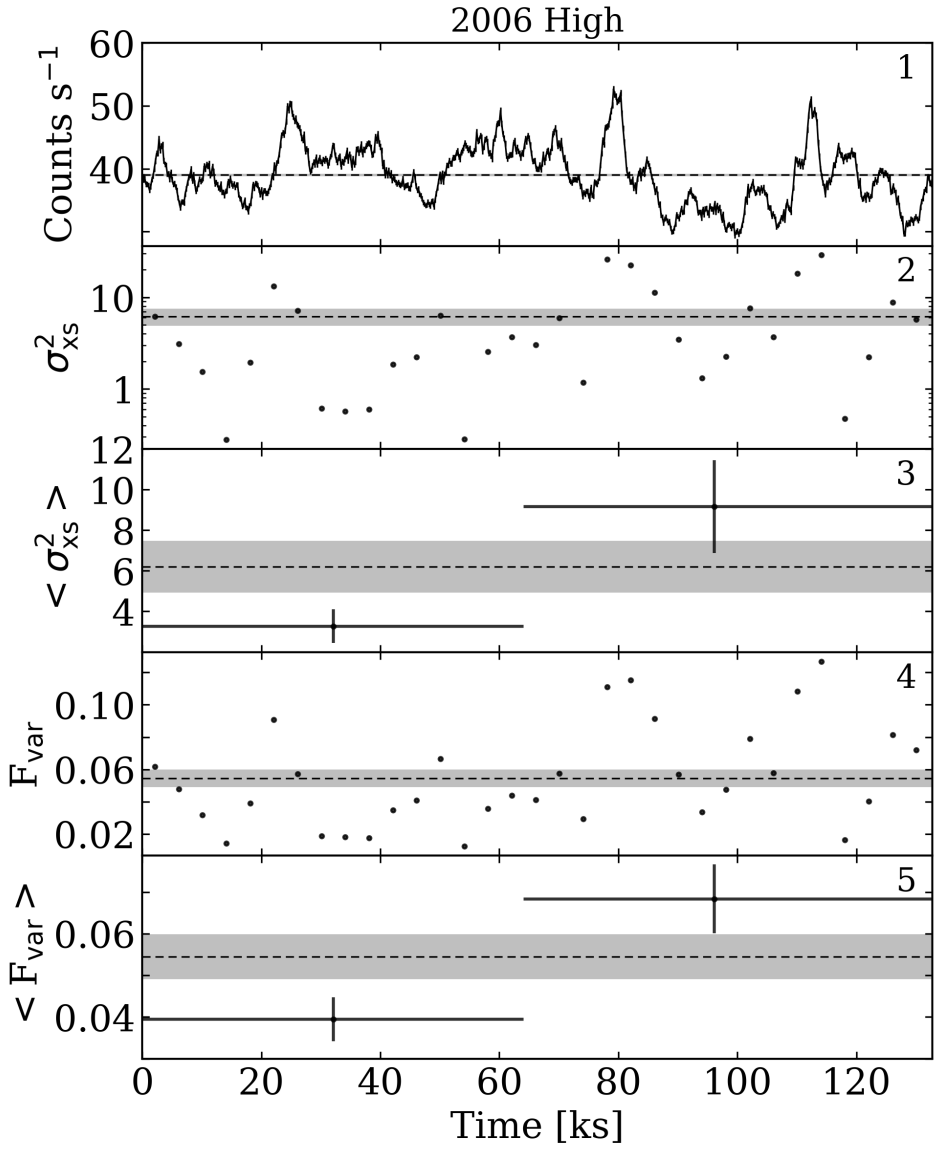

Figure 3.5: *Panel 1:* EPIC-merged light curve of 2006 High observation of Mrk 335, binned by 200s. Dashed line indicates average count rate of observation. *Panel 2:* Excess variance of the above light curve, calculated for every $N = 20$ points. Dashed line indicates average excess variance, and shaded region denotes uncertainty on the average. *Panel 3:* Excess variance averaged every $M = 16$ points. Dashed line and shaded region indicated average excess variance of the above panel. *Panel 4:* Fractional variability of the light curve, calculated for every $N = 20$ points. Dashed line indicates average fractional variability, and shaded region denotes uncertainty on the average. *Panel 5:* Fractional variance averaged every $M = 16$ points. Dashed line and shaded region indicate average fractional variability and uncertainty of the above panel.

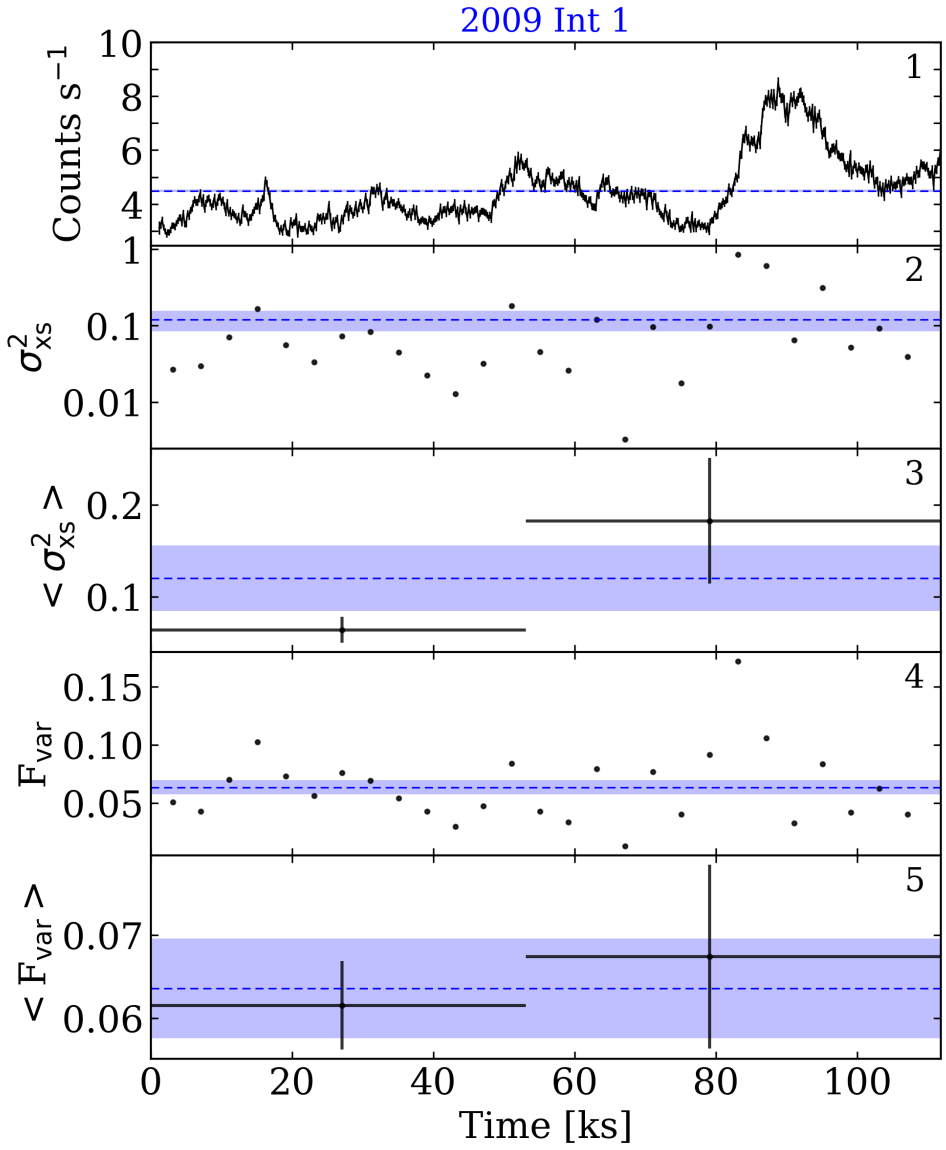

Figure 3.6: *Panel 1:* EPIC-merged light curve of 2009 Int1 observation of Mrk 335, binned by 200s. Dashed line indicates average count rate of observation. *Panel 2:* Excess variance of the above light curve, calculated for every $N = 20$ points. Dashed line indicates average excess variance, and shaded region denotes uncertainty on the average. *Panel 3:* Excess variance averaged every $M = 13$ points. Dashed line and shaded region indicated average excess variance and uncertainty of the above panel. *Panel 4:* Fractional variability of the light curve, calculated for every $N = 20$ points. Dashed line indicates average fractional variability, and shaded region denotes uncertainty on the average. *Panel 5:* Fractional variance averaged every $M = 13$ points. Dashed line and shaded region indicate average fractional variability and uncertainty of the above panel.

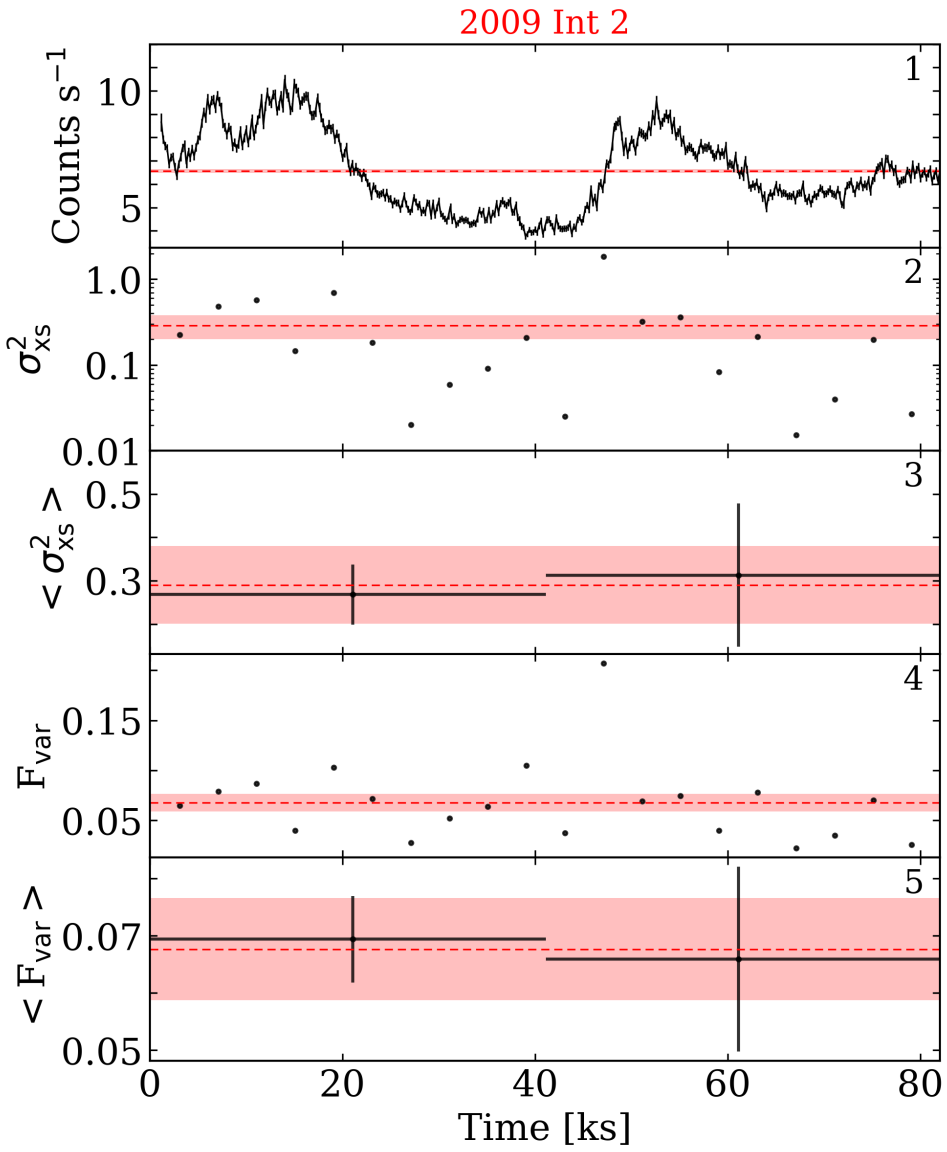

Figure 3.7: *Panel 1:* EPIC-merged light curve of 2009 Int2 observation of Mrk 335, binned by 200s. Dashed line indicates average count rate of observation. *Panel 2:* Excess variance of the above light curve, calculated for every $N = 20$ points. Dashed line indicates average excess variance, and shaded region denotes uncertainty on the average. *Panel 3:* Excess variance averaged every $M = 10$ points. Dashed line and shaded region indicate average excess variance and uncertainty of the above panel. *Panel 4:* Fractional variability of the light curve, calculated for every $N = 20$ points. Dashed line indicates average fractional variability, and shaded region denotes uncertainty on the average. *Panel 5:* Fractional variance averaged every $M = 10$ points. Dashed line and shaded region indicate average fractional variability and uncertainty of the above panel.

same figures.

These average $\langle F_{\rm var} \rangle$ values were then compared across all observations (Figure 3.8). The average of all $\langle F_{\rm var} \rangle$ values was computed and is plotted as the dashed yellow line, with one standard deviation from this average denoted by the yellow shaded region. If all of these $\langle F_{\rm var} \rangle$ values were consistent, that would be evidence of stationary behaviour. As can be seen from the figure, the first half of the 2006 High observation deviates significantly from the average, which suggest non-stationary behaviour in that portion of the observation.

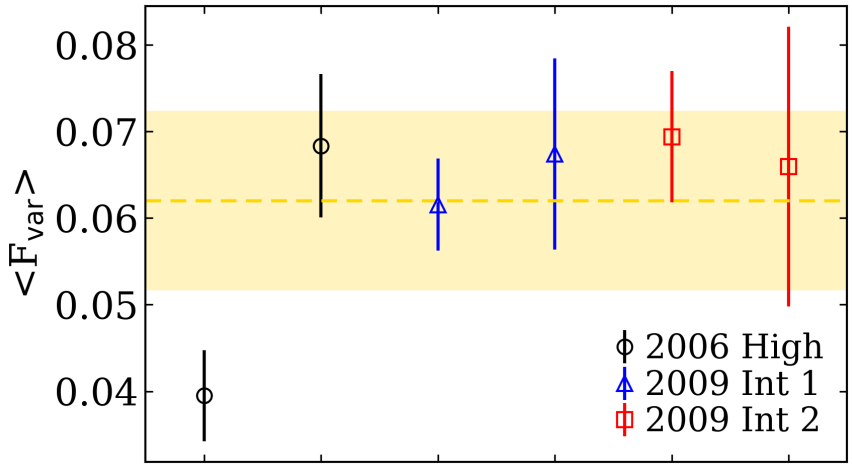

Figure 3.8: Comparison of $\langle F_{\rm var} \rangle$ values across the three observations. Average of all $\langle F_{\rm var} \rangle$ is shown by dashed line with shaded region denoting 1σ deviation from the average. All $\langle F_{\rm var} \rangle$ fall within the average save the first half of the 2006 High observation, hinting at non-stationarity for that portion of the observation.

We noted in Section 3.2.1 that a lognormal count rate distribution is a sign of stationarity. To test this for Mrk 335, broadband $(0.3 - 10$ keV) light curves binned at 100s were used to construct a histogram of counts for each observation. First, the natural logarithm was taken of the light curve, then the histogram constructed of these values. The three histograms are

shown in Figure 3.9. A Gaussian function of the form:

$$g(x) = C\frac{1}{\sigma\sqrt{2\pi}}e^{-\frac{1}{2}\left(\frac{x-\mu}{\sigma}\right)^2} \tag{3.23}$$

was fit to the histograms, where C is the normalisation, σ the standard deviation, and μ the mean. As shown in Figure 3.9, this function poorly describes all three observations. To quantify the normality of these distributions we performed an Anderson-Darling normality test (Anderson & Darling 1952). The test confirmed non-normality for all three distributions, yielding p-values of 0.0007, $< 2.2 \times 10^{-16}$, and 8.341×10^{-11} for 2006 High, 2009 Int 1, and 2009 Int 2, respectively. Thus, the count rate distributions seem to suggest non-stationarity for all three observations. However, as we will discuss later, this could be a result of insufficient frequency sampling.

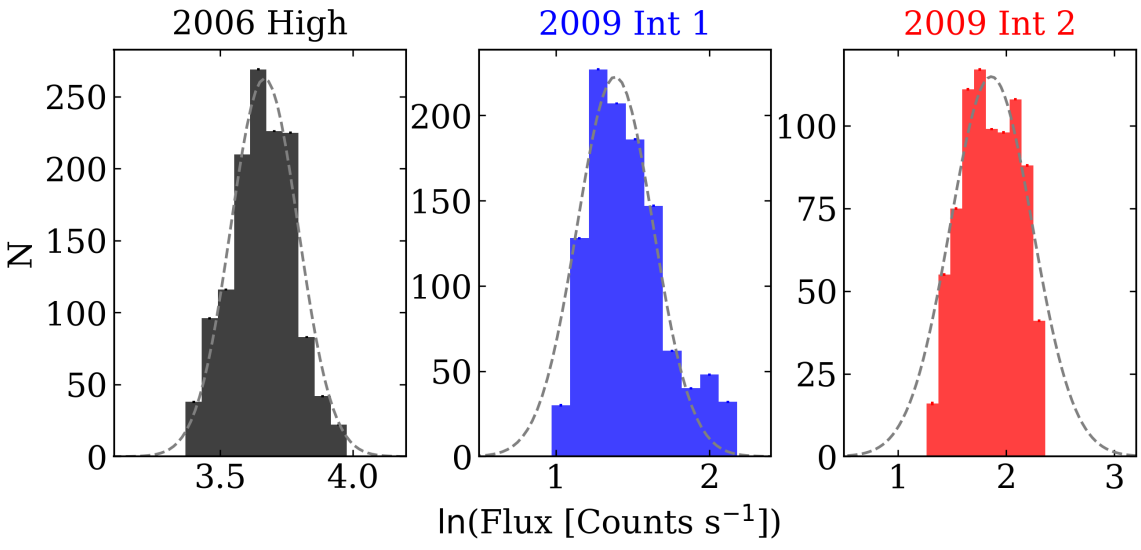

Figure 3.9: Histograms of the natural logarithm of the light curve counts for the three observations. Normal fits to the histograms are shown as dashed grey curves.

3.4.2 Power Density Spectrum

PSDs were constructed for the three observations following the recipe in Uttley et al. (2014), outlined in Section 3.2.2. They were constructed from light curves in the $0.3-10$ keV band, binned in 100s intervals. The resulting periodograms were binned using the logarithmic binning method described by Papadakis & Lawrence (1993), where each frequency bin contains a minimum of two points, and the bin width is set at $B \times f_i$, where B is some binning factor and f_i the smallest Fourier frequency in that bin (Arévalo et al. 2008b). A binning factor of $B = 1.3$ was used to construct the PSD of each observation. The binned-up PSDs are shown together in Figure 3.10. Each has been truncated where the Poisson noise starts to dominate the spectrum, at $\sim 10^{-3}$ Hz. They are plotted as Power $\times$ Frequency vs. Frequency as per the convention.

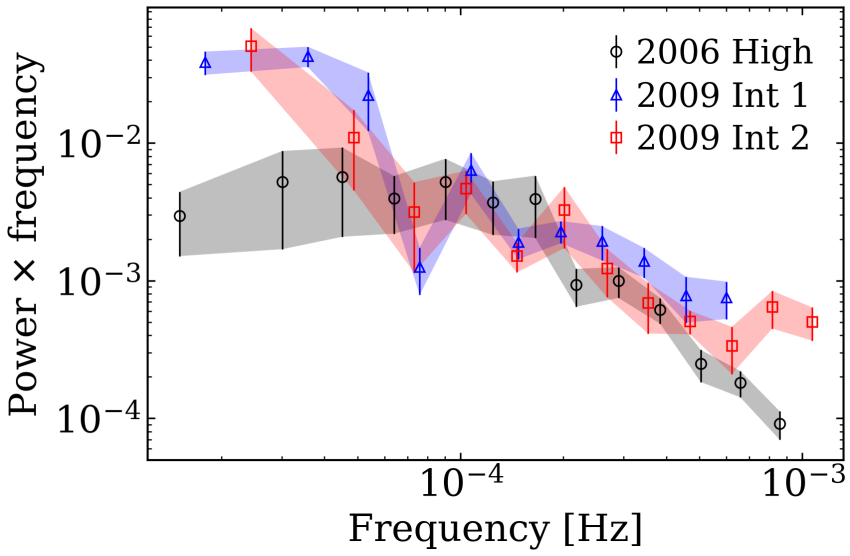

Figure 3.10: Power density spectra for the three observations of Mrk 335. PSDs were constructed from light curves binned at 100s intervals, and PSDs were binned by a factor of 1.3. The data which lie below the Poisson noise level for each observation has been omitted.

The PSDs were fit with a bending power-law model of the form:

$$P(f) = \frac{A f^{-\alpha_{\rm L}}}{1 + (f/f_{\rm b})^{\alpha_{\rm H} - \alpha_{\rm L}}} \tag{3.24}$$

from Arévalo et al. (2008b), where $\alpha_{\rm L}$ and $\alpha_{\rm H}$ represent the low- and high-frequency slopes, respectively, $f_{\rm b}$ the break frequency, and A the normalisation. The low-frequency slope was fixed to $\alpha_{\rm L} = -1$ because that is the typical slope of AGN PSDs, while $\alpha_{\rm H}$, $f_{\rm b}$, and A were left free to vary. The PSDs were fit using only the data which lies above the Poisson noise level (i.e. below $\sim 10^{-3}$ Hz). The broken power-law model was able to well-describe the 2006 High observation, as shown in Figure 3.11 (top left panel), but was unable to constrain a break frequency for the 2009 Int 1 and 2009 Int 2 observations. The break frequency for the 2006 High observation was found to be $(1.6 \pm 0.3) \times 10^{-4}$ Hz, which is in agreement with that found by Arévalo et al. (2008b) for the same observation.

Since the binned-up PSDs are not strictly Gaussian, with some bins containing < 20 data points, an alternate fitting procedure was investigated. The unbinned PSD of 2006 High was modelled with the X-ray spectral modelling software XSPEC using the Whittle statistic (e.g. Vaughan 2010; González-Martín & Vaughan 2012). The Whittle statistic (Whittle 1953; Whittle 1957) uses maximum likelihood estimation and is an approximation of a stationary Gaussian time series. It is often used for parameter estimation from a noisy signal. The fit to the 2006 High raw PSD using the Whittle statistic is shown in Figure 3.12. This fit found the break frequency to be $(1.3 \pm 0.3) \times 10^{-4}$ Hz, which is in agreement with that obtained from fitting the binned-up PSD, and so the latter was used for simplicity.

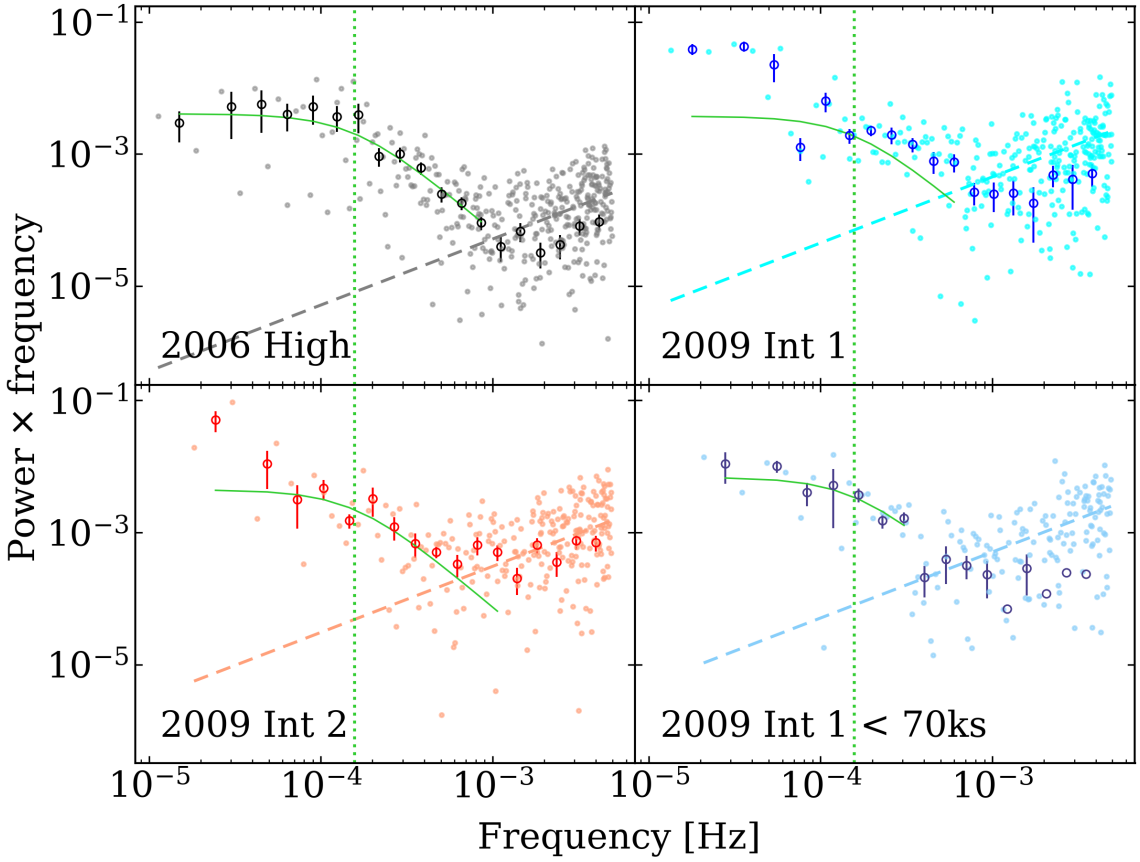

Figure 3.11: *Top left:* PSD for 2006 High observation, made from $0.3 - 10$ keV EPIC-merged light curve binned at 100s. Raw PDS is shown as grey dots, while PDS binned up with $B = 1.3$ is shown as black circles. The Poisson noise level is denoted by the grey dashed line, which starts to dominate the PSD at $\sim 10^{-3}$ Hz. Broken power-law model fit to the binned-up PSD is shown as the green curve. Data below the Poisson noise level (above $\sim 10^{-3}$ Hz) was excluded from the fit. Break frequency obtained from this fit is denoted by the vertical dotted green line. *Top right:* Same, but for 2009 Int 1 observation. The model (green curve) is that from the 2006 High observation re-normalised to the 2009 Int 1 data. *Bottom left:* Same, but for 2009 Int 2 observation, with model re-normalised to these data. *Bottom right:* Same, but for only for the 70ks of the 2009 Int 1 observation, with model re-normalised to these data.

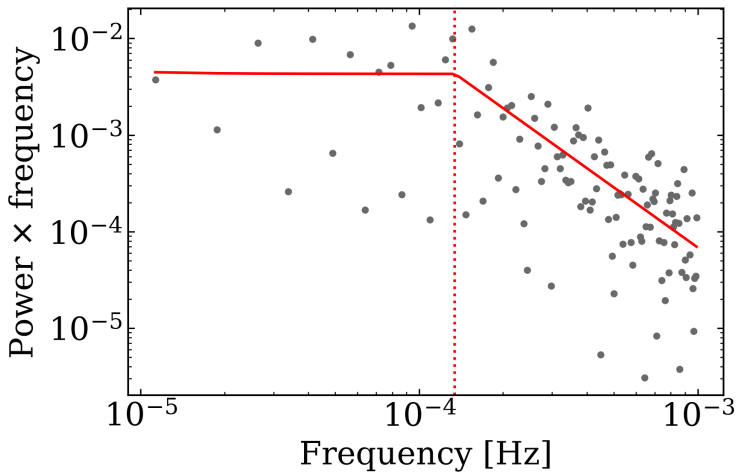

Figure 3.12: Unbinned PSD of 2006 High fit with a broken power-law using the Whittle statistic. Fit parameters were found to be consistent with those obtained from modelling the binned up PSD.

As mentioned in Section 3.2.2, a changing PSD implies non-stationarity. To check for stationarity we wanted to compare the PSDs of the three observations; however, we were unable to constrain a break frequency in the PSDs of the 2009 Int 1 & 2 observations. As such, in order to compare the PSDs of the three observations, we used the best-fit model to the 2006 High PSD and compared it to the other observations. This model was re-normalised to the 2009 Int 1 & 2 PSDs and over-plotted, preserving the break frequency and power-law indexes of the 2006 High model. The comparisons are shown in the top-right and bottom-left panels of Figure 3.11. Int 1 is very poorly fit with χ^2/dof= 96.1/10, while the fit to Int 2 is an improvement with χ^2/dof= 36.5/11.

Based on the results of Gallo et al. (2013), which found a change in the mode of variability of Int 1 at $\sim$ 70ks, a PSD of the observation was constructed using only light curve data $<$ 70ks (Figure 3.11, bottom-right panel). As can be seen from the figure, when the 2006

High PSD model is re-normalised to these data the fit is comparable (χ^2/dof= 8.74/6). As such, 2009 Int 1 $<$ 70 ks was considered separately for subsequent analyses; however, no further significant differences were noted between Int 1 & Int 1 $<$ 70ks so only results from the full observation are presented.

3.4.3 RMS Spectrum

In the manner of Jin et al. (2017), we constructed frequency-dependent rms spectra using the recipe by Arévalo et al. (2008a), outlined in Section 3.2.3. Light curves were created in the following 17 energy bands: 0.3−0.4, 0.4−0.5, 0.5−0.6, 0.6−0.7, 0.7−0.8, 0.8−1, 1−1.3, 1.3−1.6, 1.6−2, 2−2.5, 2.5−3, 3−3.5, 3.5−4, 4−5, 5−6, 6−7, 7−10 keV. For the 2006 High observation, the count rate was high enough to enable even finer energy bands to be implemented, so twice as many bands were used $<$ 5 keV. The light curves were constructed from only the EPIC pn detector (not merged) and were binned at 100s. Unmerged light curves were used because the fractional rms spectrum would need to use the response files of a single detector (more below). Two frequency ranges were explored: frequencies below the break frequency ($f < f_b$), and frequencies above the break frequency ($f > f_b$). Since the fits to the PSDs of 2009 Int 1 & 2 were unable to constrain a break frequency, the break frequency of 2006 High was used for these observations as well (1.57×10^{-4} Hz).

The normalised excess variance for the three observations is shown in Figure 3.13. For each observation there are clear differences between the spectra below and above the break frequency; this indicates a timescale dependence of the variable spectral component(s) (Arévalo et al. 2008a). At most energies, there is more variability in the frequencies below the

break, while above the break there is weak variability below ~ 1 keV which then increases with energy. The normalised excess variance spectra were used to construct the fractional rms spectra using the relation from Arévalo et al. (2008a) (see Section 3.2.3). The fractional rms spectra are plotted in Figure 3.14.

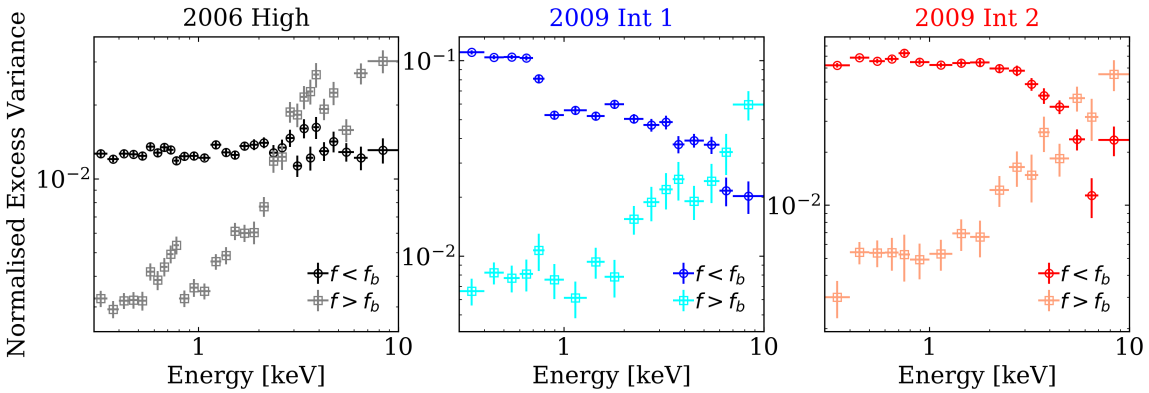

Figure 3.13: Normalised excess variance spectra for frequencies below and above the break frequency for each observation of Mrk 335.

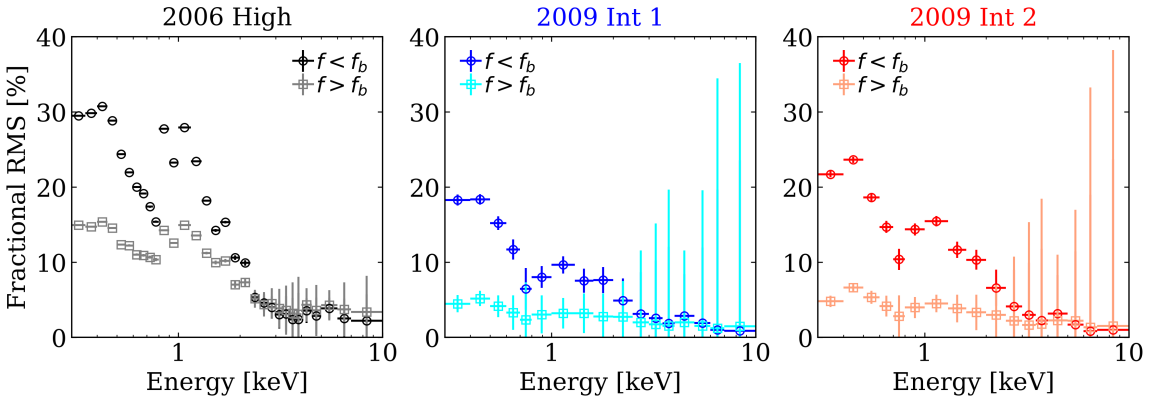

Figure 3.14: Fractional rms spectra calculated below and above the break frequency for each observation of Mrk 335.

Arévalo et al. (2008a) note that the shape of the rms spectrum is dependent on the response of the detector and so must be fitted using the same response matrices as the

time-averaged energy spectrum. As such, we multiplied the fractional rms spectrum of each observation by the time-averaged energy spectrum of the corresponding observation to obtain the absolute rms spectrum. The resolution of the rms spectrum was maintained in this process. We then put these spectra into the X-ray modelling software XSPEC and linked the response matrices using the `python` package `astropy` to manipulate the fits files. Figure 3.15 shows the absolute rms spectra convolved with the detector response. We plot the time-averaged EPIC-pn energy spectrum of each observation as well for reference. Poor signal-to-noise at high energies manifests as an absence of rms data at those energies.

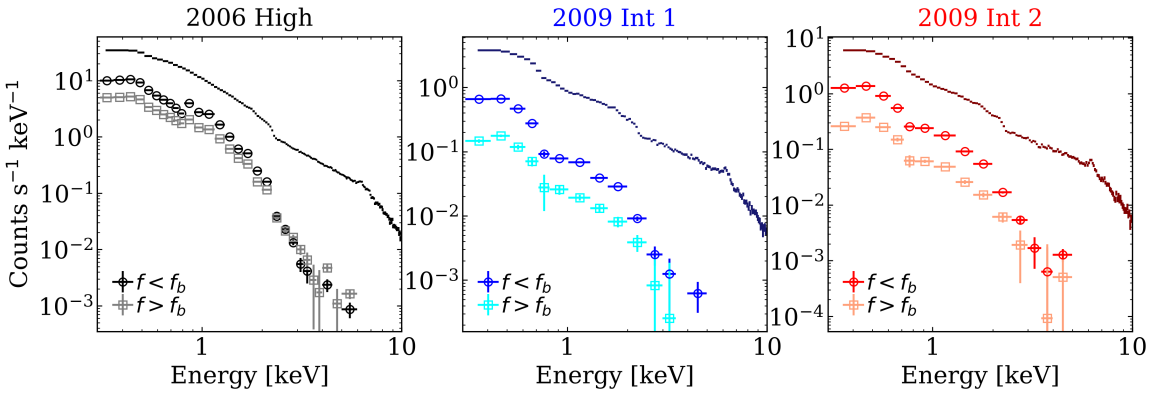

Figure 3.15: Frequency-dependent rms spectra calculated below and above the break frequency for each observation of Mrk 335. Average EPIC-pn spectrum of each observation is shown as the darkest points for reference.

The rms spectra show the spectral shape of the variable component(s) for the timescales corresponding to the frequency ranges. Qualitatively, the rms spectra of 2009 Int 1 & 2 have similar shapes for both frequency ranges, while the rms spectra of 2006 High are steeper. The small error bars on these spectra and the lack of data at higher energies make them difficult to fit with spectral models.

3.4.4 Covariance Spectrum

The recipe in Uttley et al. (2014) (outlined in Section 3.2.4) was followed to construct absolute covariance spectra for frequency ranges below and above the break frequency. The energy bands used were the same as those used for the rms spectra (see Section 3.4.3), and $0.3 - 10$ keV was used as the reference band. As was done for the rms spectrum, light curves from the EPIC-pn detector only (not merged with mos) were used so that the covariance spectrum could use the response matrices of a single detector. The covariance spectra were convolved with the detector response and put into XSPEC. Figure 3.16 shows the covariance spectra for the three *XMM-Newton* observations. The higher signal-to-noise of the covariance spectrum is evident, with data points at all energies.

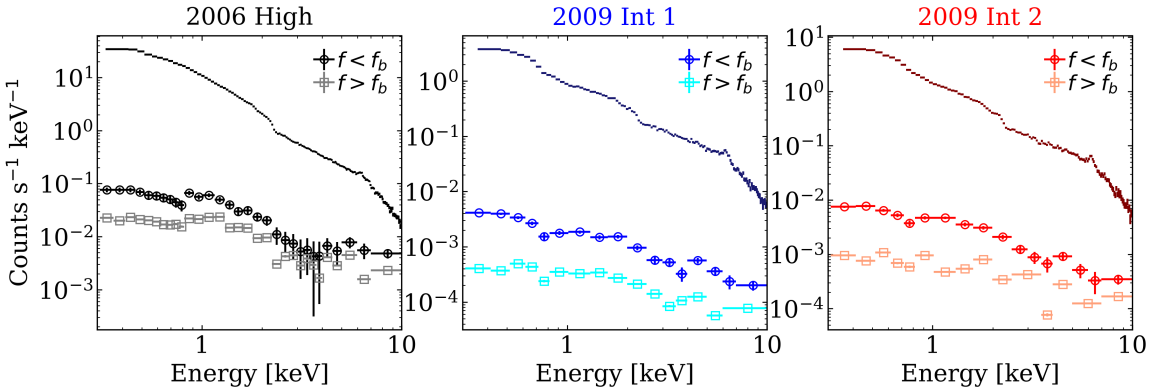

Figure 3.16: Frequency-dependent covariance spectra calculated below and above the break frequency for each observation of Mrk 335. Average EPIC-pn spectrum of each observation is shown as the darkest points for reference.

The covariance spectra show the spectral shape of the variable component(s) that are correlated with the broadband ($0.3 - 10$ keV) in a given frequency range. Qualitatively, the covariance spectra of 2009 Int 1 & 2 seem to have the same shape for both frequency ranges.

As we found with the rms spectra, the covariance spectra of 2006 High are slighter steeper than those of the 2009 Int 1 & 2. The error bars on all covariance spectra are quite small, making them difficult to fit with spectral models.

3.4.5 Lag-frequency Spectrum

Lag-frequency spectra were constructed following the recipe in Uttley et al. (2014), outlined in Section 3.2.5. They were made using the bands $x = 1 - 4$ keV and $y = 0.3 - 1$ keV in order to probe the continuum and soft excess regimes. The light curves were binned at 100s and the lag-frequency spectra were binned to maximise signal-to-noise in each bin. The lag-frequency spectra are plotted in Figure 3.17. To avoid the effects of red noise leakage we ignore frequencies corresponding to 1/3 the total light curve length. Additionally, due to low coherence (~ 0), frequencies above $\sim 5 \times 10^{-4}$ Hz are omitted.

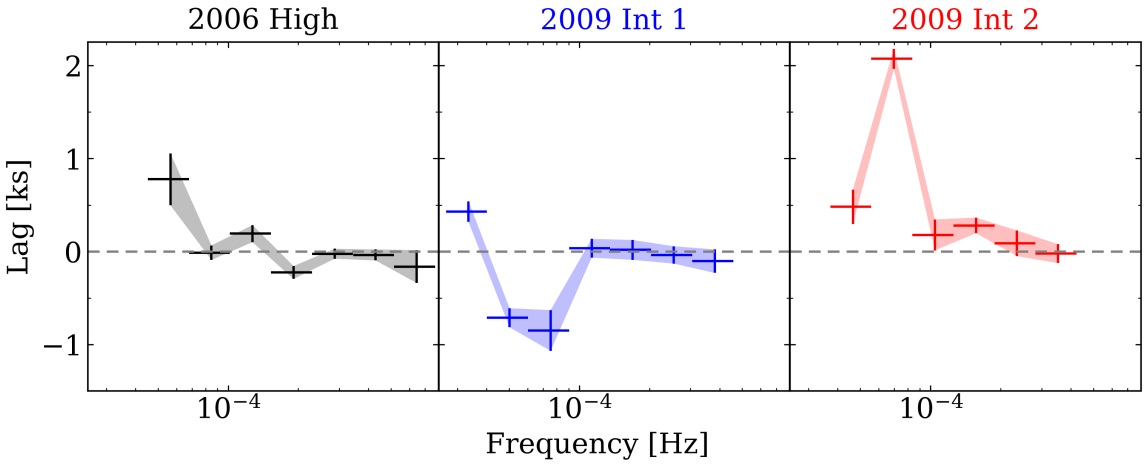

Figure 3.17: Lag-frequency spectra of Mrk 335.

The positive, low-frequency lags of the 2006 High lag-frequency spectrum can be attributed to the accretion process (e.g. Wilkins et al. 2016). Additionally, there is a higher

frequency negative lag of 225 s at $\sim 2 \times 10^{-4}$ Hz. This may be due to a time delay between the corona and disc, i.e. reverberation. 2009 Int 1 has a low frequency negative lag, which is difficult to explain, especially given how large the lag is ($\sim$ 850 s). At the same frequency, 2009 Int 2 has a very large positive lag of $\sim$ 2 ks, followed by another positive lag just above 10^{-4} Hz, which could be due to the accretion process.

3.4.6 Principal Component Analysis

A principal component analysis was performed using code made publicly available by M. Parker [2]. The spectra of the principal components for each observation are shown in Figure 3.18. The percentage of the total variability accounted for by each component is noted by the percentage in each panel. The PC spectra were constructed using spectral segments of 10 ks, and so data from $0 - 110$ ks of the 2009 Int 1 observation and data from $0 - 80$ ks of the 2009 Int 2 observation were used in this analysis. We used only data from $10 - 120$ ks for the PCA of 2006 High, as there is some background flaring at the beginning and end of the observation. This analysis identifies two significant principal components for the 2006 High observation, while 2009 Int 1 & 2 each have only one significant principal component.

The spectrum of PC 1 for 2006 High is all positive, indicating that the variability in this observation is dominated by correlated changes across all energies. This could be a result of changes in normalisation of the spectrum. The second PC of 2006 High crosses 0, indicating a variable component that is anti-correlated at high and low energies. This could be a result of changes in spectral slope, i.e. a pivoting of the spectrum. The PC spectra of 2009 Int 1

[2] `http://www-xray.ast.cam.ac.uk/~mlparker/`

& 2 are more or less consistent with PC 1 of 2006 High, suggesting that variability is driven by correlated changes across all energies.

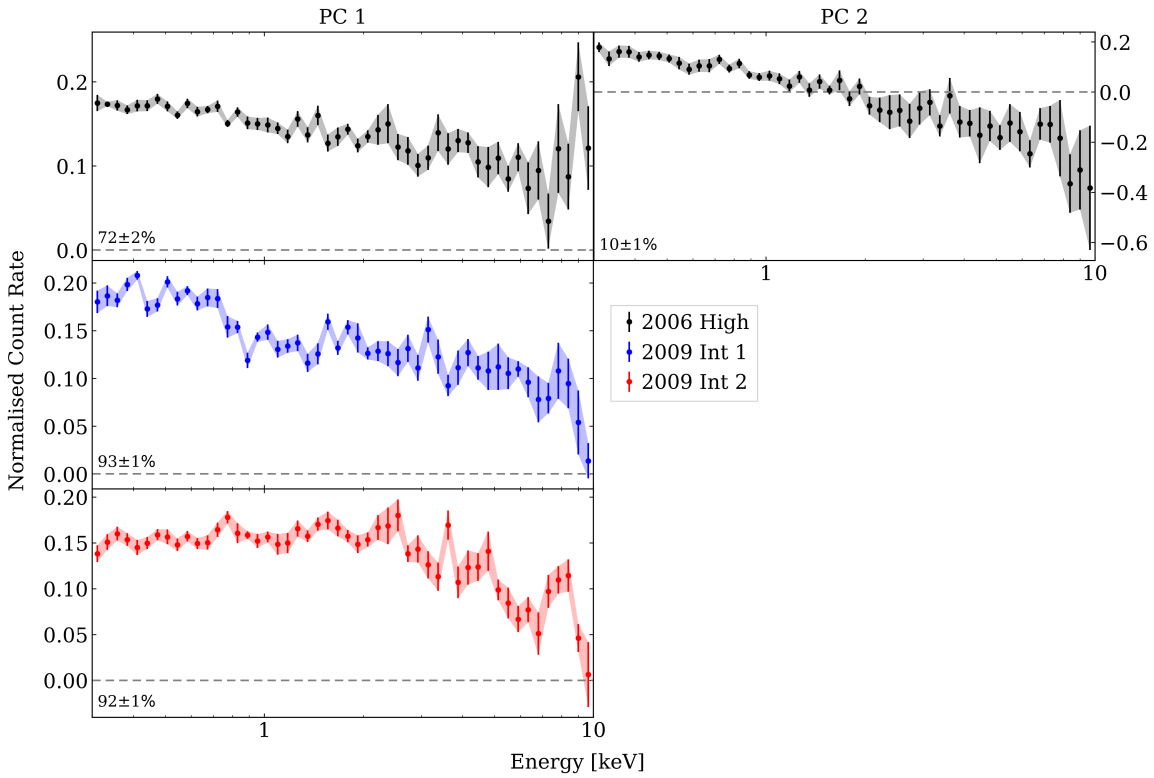

Figure 3.18: Spectra of the principal components of Mrk 335 observations. The percentage in each panel notes what fraction of the total variability each PC accounts for.

3.5 Results & Future Work

This timing study of Mrk 335 is still incomplete and requires additional analysis. We discovered hints of non-stationary behaviour, though further tests would need to be performed to confirm this. In this section we summarise our current findings and present future steps to be taken to conclude this study.

We attempted to characterise the variability of Mrk 335 by examining the average fractional variability ($\langle F_{\rm var} \rangle$) across each light curve and comparing these averages (Figure 3.8). All $\langle F_{\rm var} \rangle$ are in agreement save the first half of 2006 High, which suggests that there is non-stationary behaviour in that portion of the observation. However, these estimates of $\langle F_{\rm var} \rangle$ are not as robust as they should be, as there are less points in each average than is recommended.

As another test of stationarity, we looked at the distribution of counts for each observation. We found that the count distributions of all three observations are not well-described by a lognormal function (Figure 3.9), which seems to imply non-stationarity. However, the fact that the data are not fit well by a lognormal function does not necessarily mean that the data are not distributed lognormally; the poor fits could be the result of limited sampling. We may not be measuring to low enough frequencies due to the length of the light curve, and may not be sampling enough of the PSD to accurately determine the correct distribution. A way to determine whether the distribution is lognormal or not, or the result of poor sampling is by simulating light curves. Timmer & Koenig (1995) present an algorithm to generate artificial light curves for a given PSD. Simulating light curves that extend down to

very low frequencies as well as light curves whose frequencies extend just below the bend in the PSD (like our observations), one can compare the count distributions of the two. This will reveal if our light curves are sufficiently sampled to draw conclusions.

The PSDs of the three observations were compared to determine if there were changes in the PSD of Mrk 335 over time, which would indicate non-stationary behaviour. There are differences between the PSDs (Figure 3.10), particularly at low frequencies, however it is difficult to determine whether these differences are the result of under-sampling at these frequencies or if there is indeed non-stationary behaviour. Again, this can be examined by generating light curves as above.

In addition to analysing the three observations, we also examined the PSD of 2009 Int 1 using only data < 70 ks. This was motivated by the work of Gallo et al. (2013), who found changes occur in the spectral components at ~ 70 ks. They modelled 2009 Int 1 & 2 with a blurred reflection model (see Figure 1.3), and found that the reflected X-ray flux and the slope of the primary continuum both became variable after 70 ks, and remained variable for the duration of the observation as well as during Int 2. A model-independent analysis using flux-flux plots (Ehler 2017) corroborated these findings, noting a change in the mode of variability at ~ 70 ks in Int 1 from a simpler mode to something more complex.

We found that the best-fit model to the 2006 High PSD described the PSD of 2009 Int $1 < 70$ ks reasonably well (Figure 3.11, bottom-right panel). This seems to suggest that the variability in these two epochs are driven by the same mechanism. The PSD model of 2006 High was found to be a poor description of the 2009 Int 1 & 2 PSDs, which indicates that there are changes in the mode of variability between these epochs. However, the PSDs (2009

Int 1 & 2 in particular) could be suffering from poor sampling, especially at low frequencies. Thus, it is difficult to compare the PSDs with certainty.

By modelling the PSDs, we found consistencies between the PSDs of 2006 High and 2009 Int 1 $<$ 70 ks, implying that these epochs are driven by the same mode of variability. This result is consistent with the findings of O'Neill et al. (2007) and Gallo et al. (2013). O'Neill et al. (2007) computed the rms spectrum of the 2006 High observation of Mrk 335 and found it to be constant across all energies, implying that the variability in this epoch is driven by correlated spectral changes across all energy bands (e.g. change of power-law flux). As we discussed earlier, spectral modelling of 2009 Int 1 by Gallo et al. (2013) discovered a change in the mode of variability at 70 ks. Prior to 70 ks, they found variability to be driven only by changes in the flux of the power-law.

We considered 2009 Int 1 $<$ 70 ks for all other analyses, but found no further significant differences between it and the full observation. This could be due to the relatively short length of the observation when truncated at 70 ks, low signal-to-noise, or the fact that there is more data $<$ 70 ks than there is $>$ 70 ks.

The covariance spectrum gives the spectral shape of all variable components that are correlated with the reference band, while the rms spectrum provides the spectrum of all the variability. Both the rms and the covariance spectra have similar shapes for the 2009 Int 1 & 2 observations, while those of 2006 High appear significantly different. This suggests changes in the variable component(s) between these epochs. The next step is to model the rms and covariance spectra to determine the spectral component(s) contributing to the variability (e.g. Jin et al. 2017). So far, this has proven difficult given the small error

bars on the spectra. To obtain a more realistic estimate of the error bars on these spectra, a bootstrapping procedure can be implemented to sample different realisations of the light curves. By resampling the light curves many times (e.g. 1000) and constructing a covariance spectrum from each resampled light curve, one can obtain a better estimate of the covariance spectrum uncertainties.

The lag-frequency spectrum probes the delay of variations between two energy bands. We constructed lag-frequency spectra for the three observations using the bands $1 - 4$ keV and $0.3 - 1$ keV to probe the continuum emission and soft excess emission, respectively. The lag-frequency spectrum of 2006 High (Figure 3.17) features a positive, low-frequency lag which can be attributed to the propagation of material in the accretion process (e.g. Wilkins et al. 2016). It also includes a negative, higher frequency lag of 225 ± 70 s at 1.9×10^{-4} Hz, which is consistent with reverberation (i.e. time delay between the corona and the disc). This result is in agreement with a previous lag analysis of this observation by Kara et al. (2013), who found a negative lag of 155 ± 57 s at $\sim 2 \times 10^{-4}$ Hz.

We found that the lag-frequency spectrum of 2009 Int 1 features a large negative lag at low frequencies, while that of Int 2 contains a large positive lag at the same frequencies. These are difficult to explain, especially given how large they are, and it is possible they are artifacts of poor sampling or signal-to-noise. Kara et al. (2013) constructed a lag-frequency from 2009 Int 1 & 2 combined, and found no significant lags. We tested this and found the same, though the figure is not presented.

Our principal component analysis, which reveals the spectral shape of individual varying components, returned two significant principal components for 2006 High and one for each of

2009 Int 1 & 2. The first principal component in all three observations seem to be consistent, and indicates that variability is correlated across all energy bands. Such variability could be caused by changes in normalisation of the power-law (coronal) component. A second principal component was identified in 2006 High, indicating that anti-correlated variability between high and low energies also contributed to the variability in that observation (e.g. changes in the spectral slope of the power-law component). Moving forward, the next step would be to use these results as a starting point for modelling the covariance spectra.

Chapter 4

Conclusions

Two different analyses were performed on two Seyfert AGN in an effort to characterise their variability. On the high mass ($\sim 10^8$ $M_\odot$) type 1.5 AGN Mrk 530, time and hardness resolved spectral analysis was adopted. For the lower mass ($\sim 10^7$ $M_\odot$) narrow-line Seyfert 1 Mrk 335, a frequency-resolved timing analysis was initiated.

The spectral analysis of Mrk 530 revealed two distinct types of variability present over a single observation. A spectral state change from a soft state to a hard state, and an apparent sinusoidal variability in a narrow energy band were observed. We performed spectral modelling in an attempt to characterise the spectral state change, but were unable to determine the origin (blurred reflection, partial covering, soft Comptonisation) with current data quality. The apparent periodicity in the light curve was found to be statistically insignificant, though it is curious behaviour that would be interesting to follow-up on with additional observing time on the *XMM-Newton* and/or *NuSTAR* X-ray telescopes.

Mrk 530 would be an especially interesting source for a timing analysis, given the appar-

ent sinusoidal variability found in the light curve. However, Fourier timing methods were not applied to this observation of Mrk 530 due to the gaps in the light curve. Mrk 530 was observed with *Suzaku*, an X-ray telescope with a period of 96 min in a low-Earth orbit. This means that there are gaps in the light curve as the telescope passes behind the Earth. The light curves were binned by 96 min (5760 s) such that each orbit would be one data point in the light curve. This reduced the amount of data that could be used for robust analysis. Long, uninterrupted observations with *XMM-Newton* would produce high-quality light curves for future work.

Extensive spectral modelling has already been performed on Mrk 335 (e.g. Gallo et al. 2013; Wilkins & Gallo 2015b) so we did not pursue that with this study. While there have been timing analyses of this source (e.g. Arévalo et al. 2008b; Kara et al. 2013), our aim was to create a comprehensive timing study of all suitable observations.

We investigated whether there was evidence of non-stationary behaviour in Mrk 335, which would ascribe the observed variability to physical changes in the AGN rather than expected red noise in the accretion process. We found hints of non-stationarity using multiple timing methods, however it is difficult to determine if these results are real or artifacts of undersampling. This study needs to be further explored, namely, the generation of artificial light curves to understand the effect of poor frequency sampling, and the modelling of the covariance spectra to better understand physical components driving the observed variability.

Mrk 335 is less massive than Mrk 530 by about an order or magnitude. Studying these two AGN allows us to probe different timescales, as the physical regions of AGN scale with

black hole mass. Different processes in AGN occur on various timescales, so examining AGN with a range of masses provides a comprehensive picture of AGN over all timescales. In studying Mrk 530, we probed dynamical timescales and discovered variability in a narrow energy band that had a periodicity consistent with an orbital timescale at a radius of $\sim 10r_g$. This could suggest the presence of a hot spot of material orbiting the black hole, but this remains an open question. Our work on Mrk 335 examined multiple epochs, allowing us to look at longer timescales and changes across a few years. We found evidence of physical changes occurring in the inner black hole region, but require further testing to confirm these results.

Bibliography

Alston W. N., et al., 2019, MNRAS , 482, 2088

Anderson T. W., Darling D. A., 1952, Ann. Math. Statist., 23, 193

Antonucci R., 1993, ARA&A , 31, 473

Arévalo P., McHardy I. M., Markowitz A., Papadakis I. E., Turner T. J., Miller L., Reeves J., 2008a, MNRAS , 387, 279

Arévalo P., McHardy I. M., Summons D. P., 2008b, MNRAS , 388, 211

Arnaud K. A., 1996, in Jacoby G. H., Barnes J., eds, Astronomical Society of the Pacific Conference Series Vol. 101, Astronomical Data Analysis Software and Systems V. p. 17

Barth A. J., Stern D., 2018, ApJ , 859, 10

Bendat J. S., Piersol A. G., 1986, Journal of Sound Vibration, 106, 391

Bevington Philip. R. R. D. K., 1992, Data Reduction and Error Analysis for the Physical Sciences, second edition edn. The McHraw-Hill Companies, Inc.

Bianchi S., Matt G., 2002, A&A , 387, 76

Cash W., 1979, ApJ , 228, 939

Costantini E., Kaastra J. S., Korista K., Ebrero J., Arav N., Kriss G., Steenbrugge K. C., 2010, A&A , 512, A25

Dauser T., García J., Parker M. L., Fabian A. C., Wilms J., 2014, MNRAS , 444, L100

Dibai E. A., 1979, Pisma v Astronomicheskii Zhurnal, 5, 379

Done C., Davis S. W., Jin C., Blaes O., Ward M., 2012, MNRAS , 420, 1848

Edelson R. A., Krolik J. H., Pike G. F., 1990, ApJ , 359, 86

Edelson R., Turner T. J., Pounds K., Vaughan S., Markowitz A., Marshall H., Dobbie P., Warwick R., 2002, ApJ , 568, 610

Edelson R., Mushotzky R., Vaughan S., Scargle J., Gandhi P., Malkan M., Baumgartner W., 2013, ApJ , 766, 16

Ehler H. J. S., 2017, A Flux-Flux Analysis of Spectral Variability in Markarian 335. Saint Mary's University

Fabian A. C., Rees M. J., Stella L., White N. E., 1989, MNRAS , 238, 729

Gallant D., Gallo L. C., Parker M. L., 2018, MNRAS , 480, 1999

Gallo L. C., 2011, JRASC , 105, 143

Gallo L. C., et al., 2013, MNRAS , 428, 1191

Gallo L. C., et al., 2015, MNRAS , 446, 633

Gallo L. C., et al., 2019, MNRAS , 484, 4287

García J., et al., 2014, ApJ , 782, 76

George I. M., Fabian A. C., 1991, MNRAS , 249, 352

Gierliński M., Done C., 2004, MNRAS , 349, L7

Gierliński M., Middleton M., Ward M., Done C., 2008, Nature , 455, 369

Gondoin P., Orr A., Lumb D., Santos-Lleo M., 2002, A&A , 388, 74

González-Martín O., 2018, ApJ , 858, 2

González-Martín O., Vaughan S., 2012, A&A , 544, A80

Gonzalez A. G., Wilkins D. R., Gallo L. C., 2017, MNRAS , 472, 1932

Gonzalez A. G., Waddell S. G. H., Gallo L. C., 2018, MNRAS , 475, 128

Goodrich R. W., 1995, ApJ , 440, 141

Grier C. J., et al., 2012, ApJ , 744, L4

Grupe D., Komossa S., Gallo L. C., 2007, ApJ , 668, L111

Grupe D., Komossa S., Gallo L. C., Lia Longinotti A., Fabian A. C., Pradhan A. K., Gruberbauer M., Xu D., 2012, ApJS , 199, 28

Halpern J. P., Marshall H. L., 1996, ApJ , 464, 760

Halpern J. P., Leighly K. M., Marshall H. L., 2003, ApJ , 585, 665

Harrison C., 2014, PhD thesis, Durham University

Humphrey P. J., Liu W., Buote D. A., 2009, ApJ , 693, 822

Iwasawa K., Miniutti G., Fabian A. C., 2004, MNRAS , 355, 1073

Jin C., Done C., Ward M., 2017, MNRAS , 468, 3663

Kaastra J. S., Bleeker J. A. M., 2016, A&A , 587, A151

Kalberla P. M. W., Burton W. B., Hartmann D., Arnal E. M., Bajaja E., Morras R., Pöppel W. G. L., 2005, A&A , 440, 775

Kara E., Fabian A. C., Cackett E. M., Uttley P., Wilkins D. R., Zoghbi A., 2013, MNRAS , 434, 1129

Kendall M. G., 1975, Multivariate analysis. Griffin London

Kolb U., 2010, Extreme Environment Astrophysics. Cambridge University Press

Kollatschny W., Bischoff K., Dietrich M., 2000, A&A , 361, 901

LaMassa S. M., et al., 2015, ApJ , 800, 144

Lal D. V., Shastri P., Gabuzda D. C., 2004, A&A , 425, 99

Lal D. V., Shastri P., Gabuzda D. C., 2011, ApJ , 731, 68

Laor A., 1991, ApJ , 376, 90

Larsson J., Miniutti G., Fabian A. C., Miller J. M., Reynolds C. S., Ponti G., 2008, MNRAS , 384, 1316

Longinotti A. L., Sim S. A., Nandra K., Cappi M., 2007, MNRAS , 374, 237

Longinotti A. L., et al., 2013, ApJ , 766, 104

López-Corredoira M., Gutiérrez C. M., 2002, A&A , 390, L15

Madau P., 1988, ApJ , 327, 116

Madejski G. M., Done C., Turner T. J., Mushotzky R. F., Serlemitsos P., Fiore F., Sikora M., Begelman M. C., 1993, Nature , 365, 626

Magdziarz P., Blaes O. M., Zdziarski A. A., Johnson W. N., Smith D. A., 1998, MNRAS , 301, 179

Malkan M. A., Jensen L. D., Rodriguez D. R., Spinoglio L., Rush B., 2017, ApJ , 846, 102

Mallick L., Dewangan G. C., McHardy I. M., Pahari M., 2017, MNRAS , 472, 174

Mantz A. B., Allen S. W., Morris R. G., Simionescu A., Urban O., Werner N., Zhuravleva I., 2017, MNRAS , 472, 2877

Matt G., Perola G. C., Piro L., 1991, A&A , 247, 25

Matt G., Fabian A. C., Ross R. R., 1996a, MNRAS , 278, 1111

Matt G., et al., 1996b, MNRAS , 281, L69

Matt G., Guainazzi M., Perola G. C., Fiore F., Nicastro F., Cappi M., Piro L., 2001, A&A , 377, L31

Matt G., Guainazzi M., Maiolino R., 2003, MNRAS , 342, 422

Matt G., et al., 2014, MNRAS , 439, 3016

McHardy I. M., Koerding E., Knigge C., Uttley P., Fender R. P., 2006, Nature , 444, 730

Mickaelian A. M., 2016, in Mickaelian A., Lawrence A., Magakian T., eds, Astronomical Society of the Pacific Conference Series Vol. 505, Astronomical Surveys and Big Data. p. 3

Monje R. R., Blain A. W., Phillips T. G., 2011, ApJS , 195, 23

Nandra K., O'Neill P. M., George I. M., Reeves J. N., 2007, MNRAS , 382, 194

Narayan R., McClintock J. E., 2008, , 51, 733

Netzer H., 2013, Main components of AGNs. Cambridge University Press

Netzer H., 2015, ARA&A , 53, 365

Novikov I. D., Thorne K. S., 1973, in Black Holes (Les Astres Occlus). pp 343–450

Nowak M. A., et al., 2011, ApJ , 728, 13

O'Neill P. M., Nandra K., Cappi M., Longinotti A. L., Sim S. A., 2007, MNRAS , 381, L94

Pan H.-W., Yuan W., Yao S., Zhou X.-L., Liu B., Zhou H., Zhang S.-N., 2016, ApJ , 819, L19

Papadakis I. E., Lawrence A., 1993, MNRAS , 261, 612

Parker M. L., Walton D. J., Fabian A. C., Risaliti G., 2014, MNRAS , 441, 1817

Parker M. L., et al., 2015, MNRAS , 447, 72

Parker M. L., Miller J. M., Fabian A. C., 2018, MNRAS , 474, 1538

Pounds K., Reeves J., O'Brien P., Page K., Turner M., Nayakshin S., 2001, ApJ , 559, 181

Puccetti S., Fiore F., Risaliti G., Capalbi M., Elvis M., Nicastro F., 2007, MNRAS , 377, 607

Reeves J. N., Turner M. J. L., Pounds K. A., O'Brien P. T., Boller T., Ferrando P., Kendziorra E., Vercellone S., 2001, A&A , 365, L134

Revnivtsev M., Gilfanov M., Churazov E., 1999, A&A , 347, L23

Rodríguez-Pascual P. M., et al., 1997, ApJS , 110, 9

Ross R. R., Fabian A. C., 2005, MNRAS , 358, 211

Seyfert C. K., 1943, ApJ , 97, 28

Shakura N. I., Sunyaev R. A., 1973, A&A , 500, 33

Shemmer O., Brandt W. N., Netzer H., Maiolino R., Kaspi S., 2006, ApJ , 646, L29

Singh V., Shastri P., Risaliti G., 2011, A&A , 533, A128

Singh V., Shastri P., Ishwara-Chandra C. H., Athreya R., 2013, A&A , 554, A85

Slavcheva-Mihova L., Mihov B., 2011, A&A , 526, A43

Sobolewska M. A., Papadakis I. E., 2009, MNRAS , 399, 1597

Takahashi T., et al., 2016, in Space Telescopes and Instrumentation 2016: Ultraviolet to Gamma Ray. p. 99050U

Tanaka Y., Boller T., Gallo L., Keil R., Ueda Y., 2004, PASJ , 56, L9

Theios R. L., Malkan M. A., Ross N. R., 2016, ApJ , 822, 45

Timmer J., Koenig M., 1995, A&A , 300, 707

Urry C. M., Padovani P., 1995, PASP , 107, 803

Uttley P., McHardy I. M., 2005, MNRAS , 363, 586

Uttley P., McHardy I. M., Vaughan S., 2005, MNRAS , 359, 345

Uttley P., Cackett E. M., Fabian A. C., Kara E., Wilkins D. R., 2014, A&A Rev. , 22, 72

Vaughan S., 2010, MNRAS , 402, 307

Vaughan B. A., Nowak M. A., 1997, ApJ , 474, L43

Vaughan S., Edelson R., Warwick R. S., Uttley P., 2003, MNRAS , 345, 1271

Vaughan S., Uttley P., Markowitz A. G., Huppenkothen D., Middleton M. J., Alston W. N., Scargle J. D., Farr W. M., 2016, MNRAS , 461, 3145

Whittle P., 1953, Arkiv for Matematik, 2, 423

Whittle P., 1957, Journal of the Royal Statistical Society. Series B (Methodological), 19, 38

Wilkins D. R., 2016, Astronomische Nachrichten, 337, 557

Wilkins D. R., Fabian A. C., 2012, MNRAS , 424, 1284

Wilkins D. R., Gallo L. C., 2015a, MNRAS , 448, 703

Wilkins D. R., Gallo L. C., 2015b, MNRAS , 449, 129

Wilkins D. R., Cackett E. M., Fabian A. C., Reynolds C. S., 2016, MNRAS , 458, 200

Wilkinson T., Uttley P., 2009, MNRAS , 397, 666

Wilms J., Allen A., McCray R., 2000, ApJ , 542, 914

Woo J.-H., Kim J. H., Imanishi M., Park D., 2012, AJ , 143, 49

Zhang P., Zhang P.-f., Yan J.-z., Fan Y.-z., Liu Q.-z., 2017, ApJ , 849, 9

Zhang P.-f., Zhang P., Liao N.-h., Yan J.-z., Fan Y.-z., Liu Q.-z., 2018, ApJ , 853, 193

Zoghbi A., Fabian A. C., Uttley P., Miniutti G., Gallo L. C., Reynolds C. S., Miller J. M., Ponti G., 2010, MNRAS , 401, 2419